

Thermal and Electrical Transport Measurements in Cast and Wrought Aluminum Alloys

A Major Qualifying Project Report

Submitted to the Faculty

of the

WORCESTER POLYTECHNIC INSTITUTE



in partial fulfillment of the requirements for the
Degree of Bachelor of Science

Gyneth Campbell

Scott H. Davison

Adam J. Gatehouse

Daniel J. Mortarelli

Advisors:

Professor Diana A. Lados
Advisor

Professor Germano S. Iannacchione
Co-Advisor

Date: 2 May 2017

This report represents the work of four WPI undergraduate students submitted to the faculty as evidence of completion of a degree requirement. WPI routinely publishes these reports on its web site without editorial or peer review.

Abstract

The goals of this project were to build an apparatus for the automated measurement of thermal and electrical conductivities of metals, while developing an integrated methodology to further relate these physical properties to the materials' characteristic microstructures. Aluminum systems were selected for the study, which included both cast (A356 and 319) and wrought (6061 and 7075) alloys. The microstructures of the materials were altered via chemistry and thermal modification (heat treatment) in order to systematically study the effects of grain size, secondary dendrite arm spacing (SDAS), and morphology of secondary phases (eutectic Si particles). A DC method was employed for the thermal and electrical (4-wire) conductivity measurements. The microstructures of the alloys were quantitatively characterized using an optical microscope with image analysis. Microhardness evaluations of the aluminum matrix before and after heat treatment were also performed. Novel relationships between the alloys conductivities and their characteristic microstructural features were uniquely established.

Executive Summary

Introduction

Transport phenomena concern the exchange of mass, energy, and momentum between the systems that are being observed and studied. Studying these phenomena involves the development of mathematical models and physical understanding of the transfer of mass, energy, and momentum. This concept is present in copious aspects of engineering disciplines, such as the study of heat transfer, mass transfer, and fluid mechanics. Transport phenomena also play an inherent role in the design and application of parts used in the aerospace and automotive field, specifically thermal and electrical transport properties.

Objectives

The goals of this project were to:

- Select and study aluminum alloys that are typically used in engines and other thermally-critical automotive and aerospace applications.
- Redesign the testing apparatus and develop a testing methodology in order to evaluate the materials' thermal and electrical conductivities.
- Correlate the materials' thermal and electrical conductivities to the materials' microstructural characteristics in order to develop a relationship between the two.

Materials and Processing

Two cast and two wrought aluminum alloys were selected for this study (cast A356 and 319, and wrought 6061 and 7075). The A356 and 6061 alloys both have the same strengthening systems (Mg_2Si precipitates). Meanwhile, 319 has an Al_2Cu precipitate strengthening system. Aluminum 7075 was selected in order to study a 7000 series alloy, since they are often used for aerospace applications requiring high strength.

For cast alloys the following characteristics and their impacts on thermal and electrical conductivity were studied:

- Grain Size
- Secondary Dendrite Arm Spacing (SDAS): Low (60 μm) and high (100 μm)

- Modification of the secondary eutectic phases: Samples were chemically modified using Sr additions to determine the impact of changing eutectic Si size and shape on thermal and electrical conductivities. Adding Sr to the cast alloys decreases eutectic Si particle size and changes the particles from plate-like to coral-like structures.
- Heat treatment: The cast samples were solutionized, quenched, naturally aged for 24 hours, and then artificially aged for periods of 1.5, 4, 8, and 16 hours. The sixteen-hour age treatment provided a condition equivalent to the T6 peak strength temper.

The impact of grain boundaries on thermal and electrical flow through the material was the main point of study for the wrought alloys. Test samples were machined from rolled plates that came pre-heat treated. These heat treatments for 6061 was T651, and for 7075 was T7351.

Apparatus Design, Sample Geometry, and Testing Conditions

Part of this project was to build an improved custom apparatus based upon the design from a previous MQP team to measure the thermal and electrical resistance of various wrought and cast aluminum alloys in various as-fabricated and heat treated conditions. The new apparatus is also capable of automated testing and data collection. The new apparatus uses a new thermally insulating fixturing cell to hold the test sample that is placed inside a much larger canister to be tested in a controlled environment. The test samples were first cut from a larger cast block or a rolled plate, and then CNC machined into cylinders with a diameter of 10 mm and length of 38 mm. All of the samples ends were polished to a mirror finish for good contact in the apparatus. All the conductivity measurements were performed at room temperature, approximately 22°C. The testing conditions included as-fabricated, solutionized only (T4), and artificially aged for 1.5, 4, 8, and 16 hours. This project required the use of fundamental equations to calculate the thermal and electrical resistances of our test samples.

Fundamental Equations

Thermal Resistance (Fourier Law) in [K/W]:

$$\Delta T_{eff} = R_{eff}P = \Delta T - \Delta T^o = (R_S + R_C)(P_o - P_l) = \frac{\rho}{A}L(P_o - P_l) + R_C(P_o - P_l)$$

where: $\Delta T = T_H - T_C =$ Temperature difference between hot and cold sides (K)

$$\Delta T^o = T_H - T_C = (\text{when } P_o = 0)$$

$$P_o = I \cdot V = \text{Applied heating power (W)}$$

$$P_l = \text{Heating power leak (W)}$$

$$R_S = \text{Sample resistance [K/W]} - \text{material and geometry dependent}$$

$$R_C = \text{Contact resistance [K/W]} - \text{interface dependent}$$

Electrical Resistance (Ohm's Law) in [V/A] or [Ohms]

$$\Delta V = R_{eff}I = (R_S + R_C)I = \frac{\rho}{A}LI + R_C I$$

where: $\Delta V =$ voltage drop [V] and $I =$ current [A]

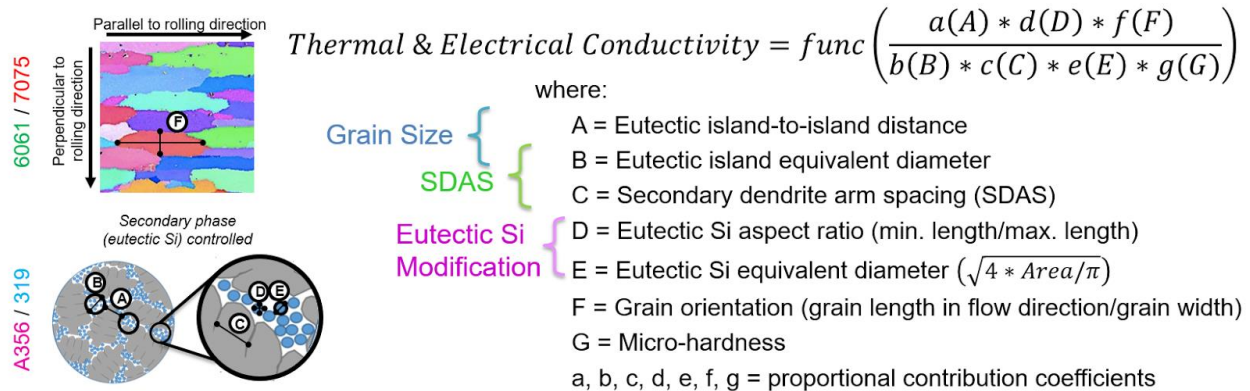
Results

After conducting thermal and electrical measurements on the test samples with various thermal and chemical modifications the following were found:

- Thermal and electrical conductivities increase with increased artificial aging time for all cast and wrought alloys.
- Thermal and electrical conductivities decrease with increasing SDAS.
- Both A356 and 319 Sr-Modified alloys have higher thermal and electrical conductivities than the unmodified ones.
- Both thermal and electrical conductivities increase with increasing grain size.
- In wrought alloys, thermal and electrical conductivities increase with the elongation of the grain in the direction of transport.

Analytical model

Based on the data and results generated, an analytical model was created to relate transport properties to microstructural characteristics as shown below.



The data show that the eutectic Si particle equivalent diameter and shape factor had the greatest effect on the thermal and electrical transport properties of the tested alloys, followed by the SDAS, grain size, and then microhardness.

Recommendations and Future Work

- Apply the developed testing methodology to other aluminum and metal alloys with different heat treatments to further understand transport phenomena.
- Perform continuous temperature dependent measurements (in-situ aging of the material within the apparatus).
- Understand the effects of in-situ aging vs. ex-situ aging followed by room temperature measurements.
- Reduce the cross-sectional area and increase the length of the test samples in order to increase the sensitivity of the measurements by increasing the samples' resistance.
- Automate test sample polishing to ensure all sample ends are consistent – uniform and flat.
- Use a thermal camera to conduct thermal transport measurements.

Acknowledgements

Our team would like to thank our advisors, Professor Diana Lados and Professor Germano Iannacchione for their guidance and advice throughout the project. Professor Lados provided indispensable knowledge on the materials processing and characterization, and guidance on developing original analytical correlations between materials' characteristics features and transport properties. Professor Iannacchione provided indispensable knowledge and guidance throughout the apparatus development and testing phases of the project.

We would also like to thank soon-to-be Dr. Anthony G. Spangenberg for his guidance and assistance throughout this project.

Finally, we would like to thank the WPI Haas Technical Education Center and its staff for assisting with the production of dozens of parts and samples for our project.

Table of Contents

Abstract.....	I
Executive Summary.....	II
Acknowledgements.....	VI
List of Figures.....	IX
List of Tables.....	XI
Chapter 1: Introduction and Objectives.....	1
1.1 Project Goals.....	1
1.2 Project Objectives.....	2
Chapter 2: Background.....	3
2.1 Basic Principles of Transport Phenomena.....	3
2.2 Current Methods for Measuring Thermal and Electrical Conductivity.....	4
2.2.1 Weideman-Franz Lorenz Law.....	5
2.2.2 Induction Heating Method.....	5
2.2.3 Searle’s Bar Method.....	7
2.2.4 Heat Flow Meter Method.....	8
2.2.5 Laser Flash Method.....	10
2.2.6 Dynamic Calorimetry.....	10
2.2.7 Method Used in this Study.....	11
2.3 Materials and Processing.....	12
2.3.1 Materials.....	12
2.3.2 Material Compositions and Heat Treatments.....	13
2.3.3 Microstructure.....	14
2.3.4 Microstructure and Mechanical Properties Relationships.....	16
2.3.5 Heat Treatment and Precipitation Strengthening.....	17
2.4 Relationship between Transport Properties and Materials’ Microstructures.....	17
2.4.1 Effects of SDAS on Conductivity.....	17
2.4.2 Effects of Heat Treatment and Aging Time.....	19
Chapter 3: Methodology.....	23
3.1 Sample Conditions.....	23
3.1.1 Cast Alloys.....	23

3.1.2 Wrought Alloys.....	25
3.2 Microstructural Analysis of Test Samples & Other Properties.....	25
3.3 Cell and Specimen Design	28
3.3.1 Original Cell Design	28
3.3.2 New Cell Design	28
3.3.3 Sample Design	30
3.4 Program Design for Thermal Measurements	30
3.5 Testing Procedure	34
3.5.1 Polishing Procedure	34
3.5.2 Cell Assembly Procedure.....	34
3.5.3 Data-Collection Protocol.....	35
3.6 Transport and Heat Transfer Equations	35
Chapter 4: Results and Discussion.....	37
4.1 Microstructural Characterization	37
4.2 Thermal and Electrical Measurements.....	39
4.2.1 Calculated Conductivities	39
4.2.2 Effect of Artificial Aging Time	39
4.2.3 Effect of Sr-Modification.....	40
4.2.4 Effect of SDAS	41
4.2.5 Effect of Grain Size.....	41
4.2.6 Effect of Grain Orientation	42
4.3 Analytical Model Relating Microstructure to Transport Properties.....	43
Chapter 5: Conclusions and Recommendations.....	44
References.....	45
Appendix A: Procedure Guide.....	47
Appendix B: Labeling System	62
Appendix C: Measurements of Microstructural Characteristics	63
Appendix D: Thermal Conductivity Measurements	67
Appendix E: Electrical Conductivity Measurements.....	70

List of Figures

<i>Figure 1: Data depicting relationship between temperature and thermal conductivity in aluminum (plotted using results from Aksöz, Öztürk, & Maraşlı, 2013).</i>	4
<i>Figure 2: Diagram of sample-magnetic field-optical furnace arrangement and heating energy focus (Bakhtiyarov et al., 2001).</i>	6
<i>Figure 3: Variation of electrical conductivity (left) and thermal conductivity (right) with temperature for pure aluminum, A319 and A356 aluminum alloys (Bakhtiyarov et al., 2001).</i>	6
<i>Figure 4: Diagram of Searle's Bar method for measuring thermal conductivity (Davison, 1997).</i>	7
<i>Figure 5: Diagram of heat flow method for thermal conductivity measurements with copper as the reference material (Mahanta & Abramson, 2010).</i>	9
<i>Figure 6: Diagram of cut-bar heat flow method for thermal conductivity measurements (TA Instruments, 2012).</i>	9
<i>Figure 7: Property requirements for jetliner and military transport applications (Starke & Staley, 1996).</i>	12
<i>Figure 8: Image of dendrites (Pace Technologies, 2014).</i>	15
<i>Figure 9: Graphical illustration of equivalent circular diameter and shape factor.</i>	16
<i>Figure 10: Dendrite arm spacing vs thermal conductivity in Al A319 (Vazquez-Lopez, 1999).</i>	18
<i>Figure 11: Dendrite perimeter vs thermal conductivity in Al A319 (Vazquez-Lopez, 1999).</i>	18
<i>Figure 12: Cooling rate vs electrical resistivity (Grandfield & Eskin, 2013).</i>	19
<i>Figure 13: Aging time vs Thermal conductivity of Al 6061 (Hernandez-Paz, 2003).</i>	20
<i>Figure 14: Variation of (left) electrical and (right) thermal conductivity with respect to temperature for pure aluminum, A319, and A356 (Bakhtiyarov et al., 2001).</i>	21
<i>Figure 15: Electrical conductivity of modified and unmodified A356 at T4 conditions at 540°C (Hernandez-Paz, 2003).</i>	21
<i>Figure 16: Distribution of equivalent diameter and shape factor of select cast alloys.</i>	27
<i>Figure 17: Comparison between new cell design (left) and old cell design (right).</i>	28
<i>Figure 18: (a) Cell bottom (b) Cell body (c) Cell top.</i>	29
<i>Figure 19: (a) Sample sabot: 0.25" tall, 1.25" outer diameter (b) Screw cap: 0.375" height and diameter.</i>	29
<i>Figure 20: Comparison between the new sample (left) and previous sample (right).</i>	30
<i>Figure 21: LabVIEW simplified flow chart.</i>	30
<i>Figure 22: Beginning of For Loop containing Stacked Sequence.</i>	31
<i>Figure 23: While Loop.</i>	32
<i>Figure 24: Reading output voltage and current.</i>	33
<i>Figure 25: Front Panel.</i>	33
<i>Figure 26: (a) Diagram of test sample. (b) Resistor equivalent</i>	36
<i>Figure 27: (a) A356-UM 500 GS 60µm; (b) A356-UM 500 GS 100µm; (c) A356+Sr 500 GS 60µm; (d) A356+Sr 500 GS 100µm.</i>	37
<i>Figure 28: (a) A356-UM 1300 GS 60µm; (b) A356-UM 1300 GS 100µm; (c) A356+Sr 1300 GS 60µm.</i>	37
<i>Figure 29: (a) 319-UM 500 GS 60µm; (b) 319-UM 500 GS 85µm; (c) 319+Sr 500 GS 60µm; (d) 319+Sr 500 GS 85µm.</i>	38
<i>Figure 30: Etched pancake grain structure of (a) 6061 and (b) 7075.</i>	38

<i>Figure 31: Thermal conductivity versus artificial aging time.</i>	<i>40</i>
<i>Figure 32: Chart showing effect of Sr-modification on thermal (left) and electrical (right) conductivity. Checkered represents modified, solid represents unmodified.</i>	<i>41</i>
<i>Figure 33: Thermal conductivity versus SDAS.</i>	<i>41</i>
<i>Figure 34: Thermal (left) and electrical (right) conductivity versus grain size. 500μm GS represented by the bar on the left of each cluster, 1300μm GS represented by the bar on the right of each cluster.</i>	<i>42</i>
<i>Figure 35: Thermal (left) and electrical (right) conductivity versus grain orientation of wrought alloys. Vertical stripes represent flow parallel to the rolling direction, horizontal stripes represent flow perpendicular to the rolling direction.</i>	<i>42</i>
<i>Figure 36: Analytical model equation relating conductivity to microstructural characteristics.</i>	<i>43</i>

List of Tables

Table 1: Chemical Compositions of Materials Tested.....	13
Table 2: A356 Sample Conditions	24
Table 3: 319 Sample Conditions	25
Table 4: Relevant Properties of Materials Tested	27

Chapter 1: Introduction and Objectives

Transport phenomena concern the exchange of mass, energy, and momentum between the systems that are being observed and studied. Studying these phenomena involves the development of mathematical models and physical understanding of the transfer of mass, energy, and momentum. This concept is present in copious aspects of engineering disciplines, such as the study of heat transfer, mass transfer, and fluid mechanics. Transport phenomena also play an inherent role in the design and application of parts used in the aerospace and automotive field, specifically thermal and electrical transport properties.

1.1 Project Goals

Materials are characterized with an intrinsic thermal and electrical conductivity based on their composition. Yet, experiments have shown that these transport characteristics are not only dependent on the composition of the material, but also on the microstructure. These same microstructural differences are part of the reason why there are various processing methods used for metal alloys. For highly conductive metal alloys, there is not extensive research available on the correlation between the high conductivity of said alloy and its microstructural properties. Thus, a need exists within the field of materials science to gain a deeper understanding of these transport phenomena, specifically how altering microstructural characteristics of the alloys affects the response of these already highly conductive materials. Developing fundamental understanding and a comprehensive model to better explain these correlations, could lead to advances in various industrial applications that use highly conductive metal alloys including the design of engines, electronic equipment, and insulation materials.

In this study, insight on material's composition, microstructure, processing and post processing conditions (e.g. heat treatment), and mechanical properties of each material tested, was provided. The methods for testing were discussed, and an improved experimental setup that could manage higher temperatures for in-situ testing was designed and built. Concurrently, the microstructure of each studied material was analyzed in order to make accurate correlations between material's microstructure and transport properties. Based on the experimental results and analysis of the data collected, original relationships between transport phenomena and microstructure were developed.

1.2 Project Objectives

The objectives of this study were to find correlations between the electrical and thermal conductivities of aluminum alloys, and their microstructure and mechanical properties. The specific alloys chosen for this study were cast (A356 and 319) and wrought (6061 and 7075) aluminum alloys. In order to develop these correlations between thermal and electrical properties and microstructure and mechanical properties of these alloys, the following objectives were set:

1. Select and study aluminum alloys typically used in engines and other thermally-critical transportation applications.
2. Redesign the testing equipment and develop a testing methodology to evaluate the materials' thermal and electrical conductivities.
3. Correlate thermal and electrical properties to materials' microstructural characteristics in order to further develop relationships between them.

Chapter 2: Background

2.1 Basic Principles of Transport Phenomena

Electrical conductivity is the ability of a material to conduct an electric current. In resistors and conductors, an electric current will flow through the material if an electric field is present. The electrical resistivity is the ratio of the electric field to the current density and can also be represented as the inverse to conductivity. These are represented by

$$\sigma = \frac{1}{\rho} = \frac{J}{E} \quad (1)$$

where ρ is the resistivity of the conductor material, E is the magnitude of the electric field, and J is the magnitude of the current density.

Conductivity varies based on material characteristics, such as whether the material is a metal, plastic, or ceramic. Metals contain a lattice of ion cores with surrounding electrons able to travel through the lattice. This outer shell of free electrons is what allows metals to conduct electrical currents. Materials with larger cross-sectional areas are better able to conduct electrons while longer materials are more resistant to carrying electrical currents. In semiconductors and insulators, donor atoms donate electrons to the conduction band or accept holes in the valence band causing a change in carrier concentration and decreasing the material's electrical resistance (Nave, 1998).

Thermal conductivity measures the rate at which heat passes through a material. If a material has a high thermal conductivity, it is able to transfer heat more readily than a less conductive material. Thermal conductance is the amount of heat which passes through a material of a known cross sectional area and length and can be found when the thermal conductivity, cross sectional area, and length are known. Thermal conductivity is represented by

$$\lambda = \frac{kA}{L} \quad (2)$$

where λ is the thermal conductance, k is the thermal conductivity, A is the cross-sectional area, and L is the length of the material.

Thermal conductivity can be affected by several factors, including temperature and electrical conductivity. In pure metals and metal alloys, electrical conductivity tends to decrease

with increasing temperature. In this instance, thermal conductivity would remain the same. In alloys however, thermal conductivity decreases as temperature increases while electrical conductivity changes very little. Thermal conductivity for polymers remains constant at low temperatures. In metals, thermal conductivity and electrical conductivity are related by valence electrons, which transfer electric current and heat (TA Instruments, 2012). One research team developed their own axial flow test apparatus and used it to test several metals, including aluminum. The relationship they found between temperature and the thermal conductivity of aluminum can be seen in Figure 1.

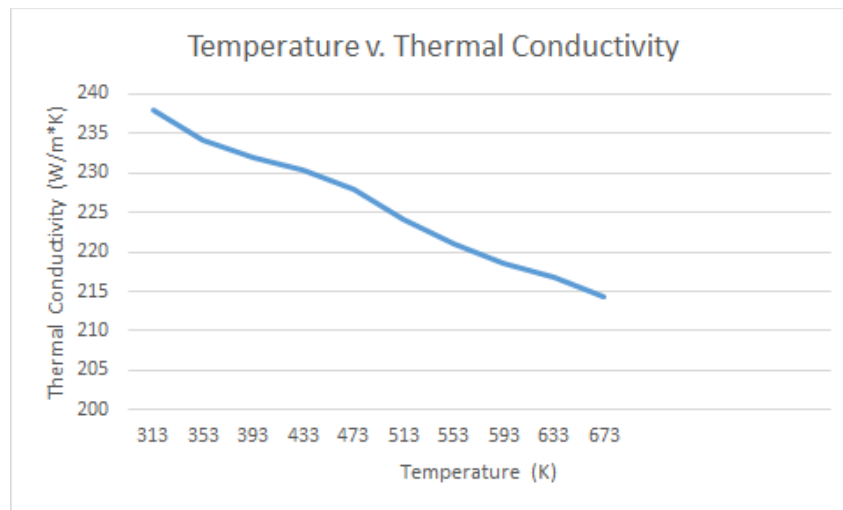


Figure 1: Data depicting relationship between temperature and thermal conductivity in aluminum (plotted using results from Aksöz, Öztürk, & Maraşlı, 2013).

The results of this study showed that the thermal conductivity of aluminum decreased as temperature increased (Aksöz, Öztürk, & Maraşlı, 2013). While understanding the principles of transport phenomena plays a key role in this project, knowing about the current methods for measuring material transport is also essential.

2.2 Current Methods for Measuring Thermal and Electrical Conductivity

Current methods for measuring the thermal and electrical conductivity of materials fall under two broad categories: steady state or non-steady state. In steady state methods, all measurements are made while the material is in a steady state, meaning that the temperature(s) or heat flow through the material are constant and independent of time. In non-steady state methods, measurements are made much more quickly and are time dependent, meaning that heat or energy

input to the material varies with time. Most methods used for measuring the thermal conductivity of materials are considered axial flow methods. In axial heat flow methods, cylindrical samples are used and the direction of heat flow during the experiment is parallel to the axis of the sample. All of the methods discussed in this section are considered axial flow methods.

2.2.1 Weideman-Franz Lorenz Law

The Weidemann-Franz-Lorenz Law is an equation that defines the relationship between the thermal conductivity and electrical conductivity of a metal, as shown in Eq. (3).

$$\frac{k}{\sigma} = LT \quad (3)$$

In this equation k is the thermal conductivity in $W/(m \cdot K)$, σ is the electrical conductivity in $\Omega^{-1}m^{-1}$, T is the temperature in K, and L is a proportionality constant called the Lorenz Number. This constant varies depending on the metal being tested and the temperature, but is in the range of $(2 \text{ to } 3) \cdot 10^{-8} W\Omega/K^2$ (Majumder & Bhattacharyya, 2008). This relationship is commonly used by researchers to calculate the thermal conductivity based on the electrical conductivity; however, many researchers including Majumder and Bhattacharyya have found that the theoretical Lorenz numbers are inaccurate, and further experimental testing must be done to determine the correct values. In an experiment to derive the thermal conductivity from the electrical conductivity of aluminum alloys at temperatures from 4K to room temperature (298K), Woodcraft discovered that using the Weidemann-Franz-Lorenz Law to determine thermal conductivity from electrical conductivity is accurate within 10% at low temperatures, but is inaccurate at room temperature (Woodcraft, 2005).

2.2.2 Induction Heating Method

Bakhtiyarov et al. conducted a study of the electrical and thermal conductivities of A319 and A356 aluminum alloys using electrical induction at high temperatures. In their experiment, they used cylindrical test samples of pure aluminum, A319, and A356 with various lengths and diameters. During the test, the sample was placed in an alumina crucible between two quartz infrared line heaters and two permanent magnets as shown below in Figure 2. The magnets generated a magnetic field so that when the crucible containing the sample was rotated about its axis, a current was produced through the sample in the axial direction. A digital micro-ohmmeter was used to measure the electrical resistance of the sample, which was then used to

calculate the electrical conductivity; their results are shown in Figure 3 (Bakhtiyarov, Overfelt, & Teodorescu, 2001). In their experiment, Bakhtiyarov et al. used the Wiedemann-Franz-Lorenz Law to determine the thermal conductivity based on the experimental electrical conductivity, however as discussed above, the Weidemann-Franz-Lorenz Law is not always reliable.

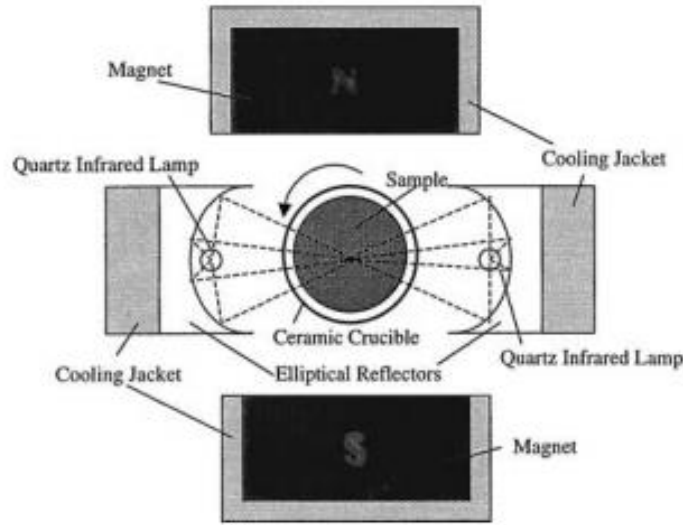


Figure 2: Diagram of sample-magnetic field-optical furnace arrangement and heating energy focus (Bakhtiyarov et al., 2001).

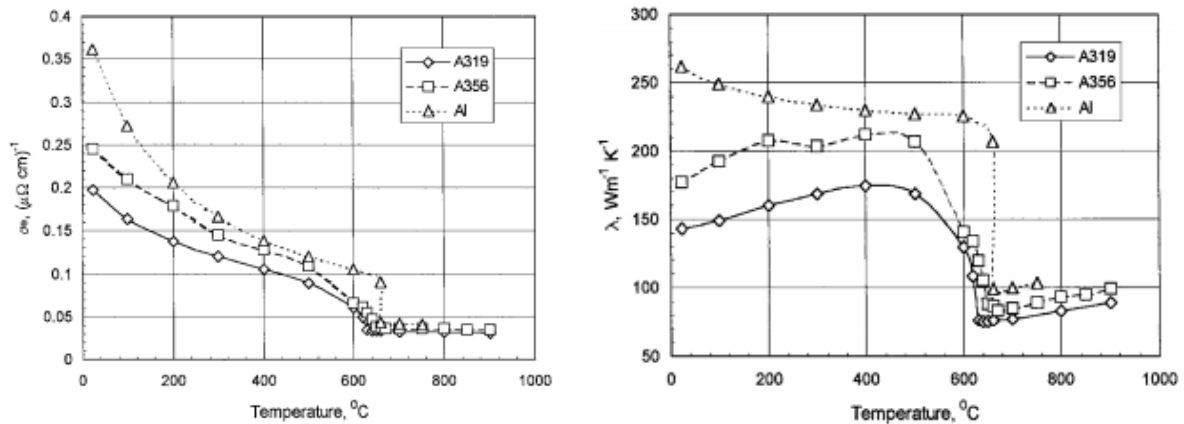


Figure 3: Variation of electrical conductivity (left) and thermal conductivity (right) with temperature for pure aluminum, A319 and A356 aluminum alloys (Bakhtiyarov et al., 2001).

2.2.3 Searle's Bar Method

One method for directly measuring the thermal conductivity of metals is the Searle's Bar method. The Searle's Bar method is a steady state method in which a cylindrical sample of the metal to be tested is encased with one end being heated by steam and the other end wrapped with coiled tubing containing cold water. Thermocouples or thermometers are placed at different points in the apparatus, two on the test sample and one each measuring the input and output temperatures of the water (Ushie et al., 2014). Figure 4 shows a diagram of the complete set up.

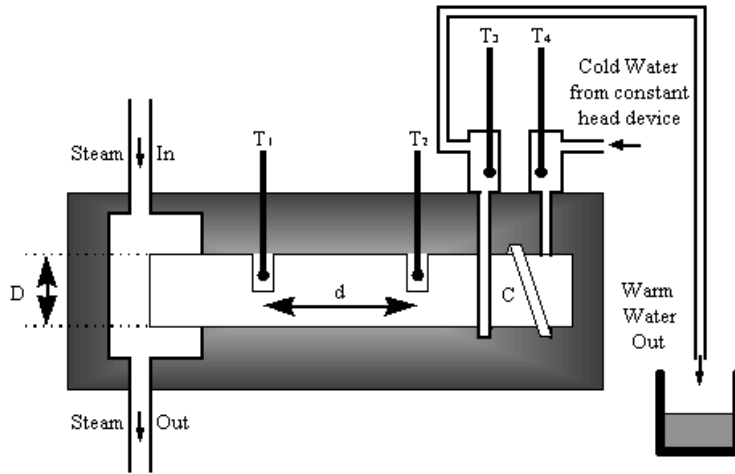


Figure 4: Diagram of Searle's Bar method for measuring thermal conductivity (Davison, 1997).

After the material reaches steady state and the temperatures are all constant, the temperature at each site is recorded and the following equations used to calculate the thermal conductivity of the test material (Ushie et al., 2014):

$$Q = \frac{-kA(T_1 - T_2)}{d} t \quad (4)$$

where Q is the heat applied to the bar in J over time t in seconds, k is the thermal conductivity of the material in $W/(m \cdot K)$, A is the cross sectional area of the bar in m^2 , T_1 and T_2 are temperatures in K or $^{\circ}C$, and d is the distance in m between the thermometers. In the other equation,

$$Q = mc(T_3 - T_4) \quad (5)$$

where, Q is the heat applied to the bar in J over time t in seconds, m is the mass flow rate of the water in m^3/s , c is the specific heat capacity of water equal to $4190 \text{ kg}^{-1}K^{-1}$, and T_3 and T_4 are

temperatures in K or °C. By setting these equations equal to each other, the thermal conductivity of the material can be found to equal the following equation, substituting $A = \pi D^2/4$ where D is the diameter of the bar:

$$k = \frac{4mcd(T_3 - T_4)}{\pi D^2(T_1 - T_2)t} \quad (6)$$

Ushie et al. also discusses the Ingen Housz method for measuring thermal conductivity, however they express that based on their findings this method is unreliable and inaccurate. The Ingen Housz method involves melting wax by heating metal samples and by comparing the length of wax melted on a test sample with the length of wax melted on a sample with known thermal conductivity a relation can be used to calculate the unknown thermal conductivity. Since this is an indirect method and the values were outside of theoretical ranges for all samples tested, Ushie et al. dismissed this method of measurement and recommended the use of the Searle's Bar method.

2.2.4 Heat Flow Meter Method

Another common method for measuring the thermal conductivity of a material is the guarded or unguarded heat flow meter method. In this method, a cylindrical sample is held in line with a reference sample of known thermal conductivity. There are two ways to conduct this test, the first involves only one reference material with an electric heater at one end and the unknown sample at the other end, at the other end of the unknown sample is a heat sink (shown in Figure 5 below). The second way to conduct this test is to place a reference material on both ends of the unknown sample and the heater at the other end of one reference material and the heat sink at the opposite end of the second reference material (shown in Figure 6 below), this is referred to as the cut-bar heat flow method. In either case the materials are held together with an axial load, and conductive film is sometimes placed between materials to create a better contact surface (Mahanta & Abramson, 2010).

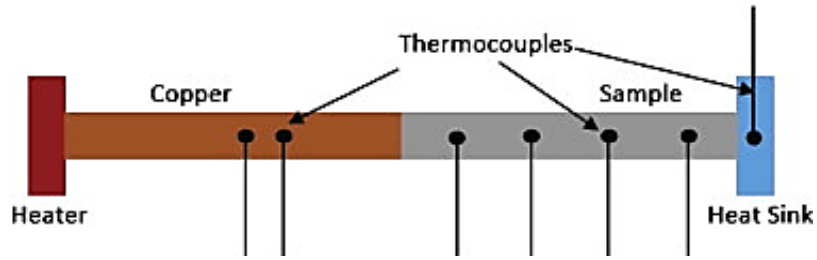


Figure 5: Diagram of heat flow method for thermal conductivity measurements with copper as the reference material (Mahanta & Abramson, 2010).

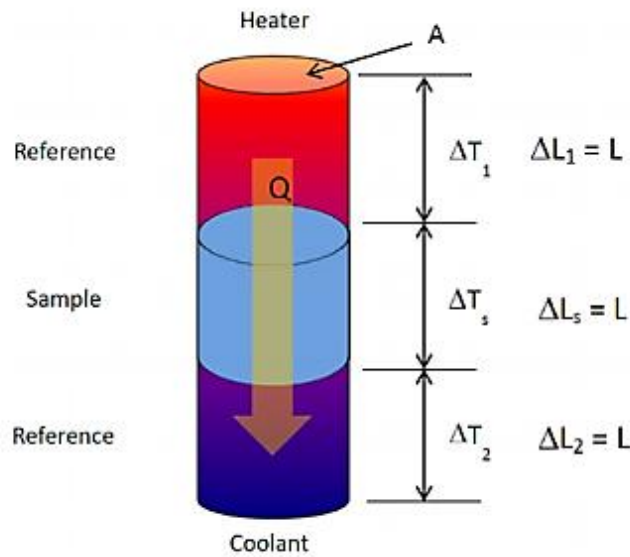


Figure 6: Diagram of cut-bar heat flow method for thermal conductivity measurements (TA Instruments, 2012).

Measurements in this method are typically done at steady state, although heat is still flowing it is at a constant rate and the temperature of the material remains constant. The temperature at both ends of the sample can be extrapolated using the temperatures, length, and known thermal conductivity of the reference material. Using this temperature drop along the length and the dimensions of the sample, the thermal conductivity can be calculated (Mahanta & Abramson, 2010). This method, and in particular the cut-bar heat flow meter method, have been found to be inaccurate when used outside of specific conditions. When the surrounding temperature becomes very high, or the temperature of the heated end is more than 10K from the surround temperature measurements become less accurate. Errors are primarily related to radial heat loss from the sample, this issue becomes exacerbated by the previously mentioned conditions (Xing, Jensen, Ban, & Phillips, 2011).

2.2.5 Laser Flash Method

The laser flash method is a non-steady state, non-contact method of measuring thermal conductivity. The sample is loaded into a chamber, a short pulse from a laser is used to heat one end of the sample, and the temperature at the other end is recorded with an infrared thermometer (Zajas & Heiselberg, 2013). By analyzing the recorded temperature versus time graph, the thermal diffusivity can be determined using Eq. (7):

$$a = 0.1388 * \frac{l^2}{t_{50}} \quad (7)$$

where a is the thermal diffusivity in mm/s^2 , l is the thickness of the sample in mm, and t_{50} is the time in seconds it takes for the end to reach half of its maximum temperature. Using the thermal diffusivity, thermal conductivity can be calculated, Eq. (8), as follows:

$$\lambda = a * c_p * \rho \quad (8)$$

where λ is the thermal conductivity in $\text{W}/(\text{m}^*\text{K})$, a is the thermal diffusivity in mm/s^2 , c_p is the specific heat capacity in $\text{J}/(\text{g}^*\text{K})$, and ρ is the density in kg/m^3 .

2.2.6 Dynamic Calorimetry

One group of researchers measured the thermal conductivity of the SAV-1 aluminum alloy. It is a ternary system alloy of Al-Mg-Si with the most common phases being, $\alpha(\text{Al})+\text{Mg}_2\text{Si}+\text{Si}$. The alloy is commonly used in various components for nuclear reactors, even in spite of its low melting temperature, because its high thermal conductivity allows it to be used under significant thermal (Nielsen (ed.), 1979). This group's experiments were performed using the dynamic calorimeter IT- λ -400 to determine the thermal conductivity of SAV-1 in the temperature range of 290-490 K. The results were calculated based on the height and cross sectional area of each sample and the temperature difference in the sample and a heat sink (Abdukadyrova et al., 2014). The following relation was used (Denisova & Shak, 2005):

$$\lambda = \frac{n_t H K_h}{n_0 S (1 + \sigma_c)} \quad (9)$$

where n_t and n_o are the temperature differences between the heat sink and sample, respectively. H is the sample height. K_h is the thermal conductivity of the heat sink rod. S is the area of a transverse section of the sample. σ_c is a correction for the heat capacity. Pure copper was used as a standard reference measurement. Their data for SAV-1 concluded that, within their experimental temperature range, this alloy exhibited a rise and fall of thermal conductivity which can be contributed to resonance scattering of phonons due to the Debye Temperature being around 390 K because the lattice thermal conductivity becomes comparable to the electronic conductivity. Their data also concluded that the thermal conductivity of SAV-1 decreased with increasing temperature assuming the absence of resonance scattering phonons.

Studying these different techniques of thermal and electrical conductivity measurement helped in the creation of our own test apparatus. We also observed data from these experiments to understand the expected behavior of the alloys tested in this study.

2.2.7 Method Used in this Study

The method used in this study is similar to the heat flow meter method. A cylindrical sample specimen is clamped between two thin copper pucks inside of a thermally and electrically insulating cell. The bottom copper puck is heated by passing a current through a resistance wire attached to the bottom of the puck. Enough power is applied for both ends of the sample specimen to change temperature, while still having a measurable difference in temperature between them. The contact resistance between the sample and pucks and the power leak from the system are determined from Eq. 10 and a sample of known thermal resistivity. This same equation is then used to calculate the thermal resistance of samples with unknown resistivity. The calculated thermal resistance of the sample and the sample dimensions are substituted into Eq. 11 to calculate the thermal resistivity of the material.

$$\Delta T - \Delta T_0 = (R_s + R_c)(P_o - P_l) \quad (10)$$

RS = Sample Resistance
 RC = Contact Resistance
 PO = Applied Heating Power
 PL = Heating Power Leak

$$R = \frac{\rho L}{A} \quad (11)$$

R = Resistance of sample
 ρ = Conductivity of sample
 L = Length of sample
 A = Cross sectional area of sample

2.3 Materials and Processing

To study and understand relationships between material microstructure and thermal and electrical transport, a thorough understanding of the materials being studied is needed. This section provides information on the alloys selected for testing, including composition, processing, microstructure, heat treatments, and relevant properties.

2.3.1 Materials

For this study two cast (A356 and 319) and two wrought (6061 and 7075) aluminum alloys were chosen. These materials were selected due to their common use in the transportation industry. Figure 7 summarizes requirements for materials for primary structural applications in subsonic aircraft. As aircraft technology developed, aluminum alloys became one of the primary materials for structural components of aircraft since the 1930s (Starke & Staley, 1996). One of the goals of this project is to provide more insight of these materials' ability to transport heat and electricity, and how microstructure and processing affects the transport phenomena.

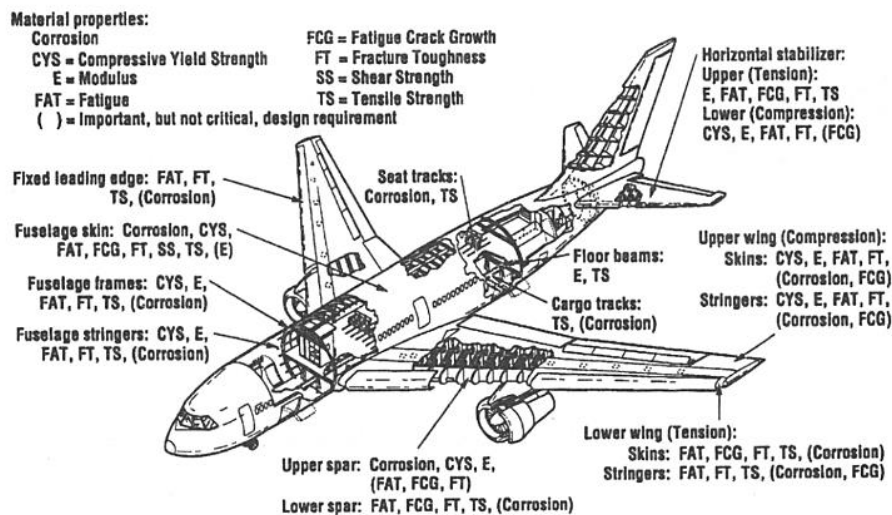


Figure 7: Property requirements for jetliner and military transport applications (Starke & Staley, 1996).

Both cast and wrought aluminum alloys were chosen for this project due to their use in both ground and air transportation for various structural and engine applications. Wrought products have been used for primary aircraft structures, and both cast and wrought products have been used for secondary aircraft structures, which are considered structures whose failure would not endanger the aircraft (Starke & Staley, 1996). Also, the cast alloys have been used for automotive engines.

2.3.2 Material Compositions and Heat Treatments

The materials under consideration included both cast and wrought aluminum alloys. These are all common materials in the automotive and aerospace industry. Table 1 lists the chemical compositions by weight percentage for each studied material.

Table 1: Chemical Compositions of Materials Tested

Composition [wt%]										
Material	Al	Cr	Cu	Fe	Mg	Mn	Si	Ti	Zn	Other
356 (Al-Si-Mg)	91.1- 93.2	0	<0.20	<0.15	0.30- 0.45	<0.10	6.5- 7.5	<0.20	<0.10	<0.15
319 (Al-Si-Cu-Mg)	83.8- 91.5	0	3.0- 4.0	<1.0	<0.10	<0.50	5.5- 6.5	<0.25	<3.0	<0.50
6061 (Al-Mg-Si)	95.8- 98.6	0.04- 0.35	0.15- 0.40	<0.70	0.80- 1.2	<0.15	0.40- 0.80	<0.15	<0.25	<0.15
7075 (Al-Zn-Mg-Cu)	87.2- 89.9	0.18- 0.28	1.2- 2.0	0.50	2.1- 2.9	0.30	0.40	0.20	5.1- 6.1	<0.15

(MatWeb, 2016; The Aluminum Association, 2015)

The wrought aluminum alloys were obtained with tempers commonly applied to these alloys when used in aerospace applications: 6061-T651 and 7075-T7351. T6 is one of the most common tempers, and it is known as the peak strength temper. In the T7 temper, the alloy is overaged; this is usually done to stabilize the microstructure or to improve corrosion resistance of the material. The 5 following the last digit for age-hardening tempers indicates the stress relieving deformation. The digit following the 5 indicates the type of stress-relieving, the numeral 1 referring to stretching (Starke & Staley, 1996). The cast aluminum alloys have been studied in as-cast as

well as naturally and artificially aged conditions. Aging times for the artificially aged samples are 1.5, 4, 8, and 16 hours.

2.3.3 Microstructure

The two main classes of aluminum selected for this experiment were wrought and cast alloys. Wrought 6061 alloys have low Si content and are grain size/orientation controlled, while the cast alloys (A356 and 319) have a higher silicon content, and are characterized by a dendritic structure within the α -Al regions, as well as secondary eutectic Si particles, which have a significant effect on the thermo-physical properties of the material. Aluminum 6061 has a pancake-shaped grain structure (i.e., primary α -Al grains that are significantly longer in length than in thickness), and a Mg-Si strengthening precipitate system.

Similar to the 6061, the wrought 7075 aluminum alloy also contains pancake-shaped grains. The grains are made up of an α -Al matrix with zinc-containing strengthening precipitates when solution treated aged (Harrison, Crawford, Janardhana, & Clark, 2011). Due to the rolling during processing, the grains tend to be elongated in the direction of rolling, with grain boundaries and inclusions forming continuous lines rather than an even dispersion that would be present without the rolling. The elongation may decrease as the material undergoes different heat treatments and could be removed altogether depending on the initial aspect ratio after rolling and the extent and intensity of the heat treatments.

Cast 319 alloys has just like A356 both primary and secondary structures, an α -Al matrix and eutectic phases, including secondary eutectic Si particles with different morphology. This alloy has an Al-Cu precipitate strengthening system. A356 has a similar structure to 319 in that it has an α -Al matrix and eutectic phases. However, A356 has the same strengthening precipitate system as 6061, but different than that of the 319.

2.3.3.1 Dendrite Arm Spacing

During the solidification of cast metal alloys, different types of microstructures may form. These may have different chemical compositions and structures within the overall alloy. The nature of these microstructures is due to the thermal history and any processing done on the material, as well as the overall chemical composition of the alloy. Dendrites, as seen in Figure 8, is one of the many microstructural features that form.



Figure 8: Image of dendrites (Pace Technologies, 2014).

Dendrites result from the geometric growth of metal crystals within a cooling alloy. These crystals have a tendency to grow with specific orientations, creating multidirectional branches, and resembling a type of fractal growth, or a tree (Collaboration for Nondestructive Testing Education, 2012). The large central branches are called primary branches, with secondary branches offshoots of the primary, and tertiary off shooting from the secondary, and so forth. There are many ways to characterize dendrites, but the most common quantities used to describe them are the arm spacing, cell interval, and cell size. Arm spacing refers to the distance between branches within the dendrite. Hence secondary dendrite arm spacing would refer to the distance between adjacent secondary branches. The cell interval of a dendrite refers to the distance between adjacent dendrite cells, essentially the spacing between primary dendrites branches on adjacent dendrites. Lastly, dendrite cell size refers to the characteristic size of a single dendrite cell, typically expressed as the width of the dendrite, but may be characterized with other physical measurements in certain cases (Kaufman & Rooy, 2004).

2.3.3.2 Secondary Particle Size

Secondary particle size (eutectic Si particles in the cast alloys studied, as further discussed in Section 4.1) also affects material properties. Two parameters are considered for their characterization, equivalent circular diameter and shape factor. These parameters are calculated as:

$$Eq. Dia. = \sqrt{\frac{4 * Area}{\pi}} \quad (12)$$

$$Shape Factor = \frac{4 * \pi * Area}{(Convex hull perimeter)^2} \quad (13)$$

These are illustrated graphically in Figure 9. In Figure 9(a), the diameter of the circle is the equivalent circular diameter, and in Figure 9(b) the ratio of the lengths of the solid line to the dotted line is the shape factor.

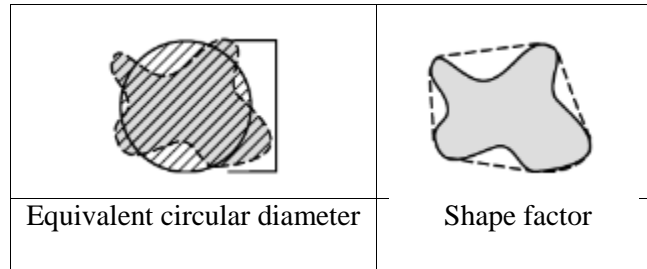


Figure 9: Graphical illustration of equivalent circular diameter and shape factor.

Shape factor is better described by a distribution than a single number. Values close to 1 describe a particle that is nearly circular, and values close to 0 describe an elongated particle.

2.3.4 Microstructure and Mechanical Properties Relationships

In this project, it is of interest to see how the microstructure of these alloys affects the thermal and electrical transport of these materials. Hence, it is important to understand how microstructural features affect properties of these alloys. The mechanical properties of aluminum alloys can vary widely based upon an alloy's microstructural characteristics. For example, aluminum alloys 6061-T6 and 356-T6 both have very similar chemical compositions, but the wrought alloy has higher tensile strength and yield strength compared to its cast counterpart. This difference is attributable to the microstructural differences between wrought and cast alloys.

In aluminum alloy AA6061-T6 tests were conducted by Toozandehjani et al. to correlate the mechanical properties of the alloy with its microstructure at various durations of heat treatments (Toozandehjani et al., 2015). What they found was that the mechanical properties improved between the as-fabricated sample up to the sample which received two hours of heat treatment. After the two-hour heat treatment, mechanical properties declined. This is the result of over aging the alloy, causing larger precipitates of Mg and Si to form and, after extended overaging.

2.3.5 Heat Treatment and Precipitation Strengthening

Precipitation strengthening or precipitation hardening is a technique to increase the yield strength of malleable metals such as aluminum. Precipitation strengthening increases the strength of the metal alloy by forming very small and uniformly dispersed second-phase particles within the original phase matrix. These particles act to impede dislocation movement, thereby strengthening the alloys. For an alloy to be able to be precipitation strengthened there must be a terminal solid solution with a decreasing solubility as temperature decreases. Usually the alloy is heated first above the solvus temperature until a homogeneous solid solution is formed. Afterward the alloy is quenched, or rapidly cooled. Quenching forms a supersaturated solid solution, which does not revert to an equilibrium structure. The atoms do not have time to diffuse to potential nucleation sites and due to this precipitation does not occur. In the final step, aging, the supersaturated solid solution is heated below the solvus temperature to form finely dispersed precipitates (Key to Metals AG, 2010).

2.4 Relationship between Transport Properties and Materials'

Microstructures

Materials' microstructures influence their thermal and electrical conductivities. Microstructural features can be altered in various ways, and each microstructural characteristic will contribute to the material's conductivities. The ways in which the microstructure of the material can be altered include chemical composition, cooling rate, and length of artificial aging. These alter the Secondary Dendrite Arm Spacing (SDAS), morphology and distribution of secondary phases, and the microhardness, which then affect the thermal and electrical conductivities of the material.

2.4.1 Effects of SDAS on Conductivity

A study featured in the Journal of Materials Research from Cambridge University explored the relationship between dendrite properties and thermal conductivity (Vazquez-Lopez, 1999). The study looked at the effects of both SDAS and the integral dendrite perimeter on the thermal conductivity. Integral dendrite perimeter is a function of the cell size and also the dendrite spacing, together they both contribute to the overall perimeter of the dendrite cell. The study's experiment found that as the secondary dendrite arm spacing increased, the thermal conductivity of the

material decreased, as shown in Figure 10. It was also found that as the perimeter of the dendrite cell increased, the thermal conductivity increased as well, Figure 11. Both results were found to have a fairly linear result as to the slope of the plotted data points. Therefore, currently these models use empirically generated equations rather than using the microstructures of the individual alloy system.

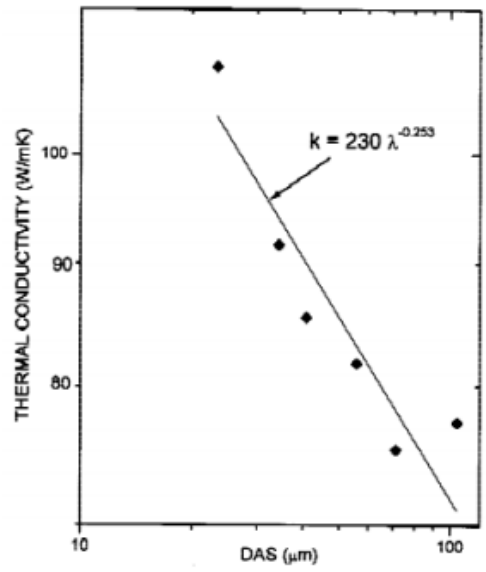


Figure 10: Dendrite arm spacing vs thermal conductivity in Al A319 (Vazquez-Lopez, 1999).

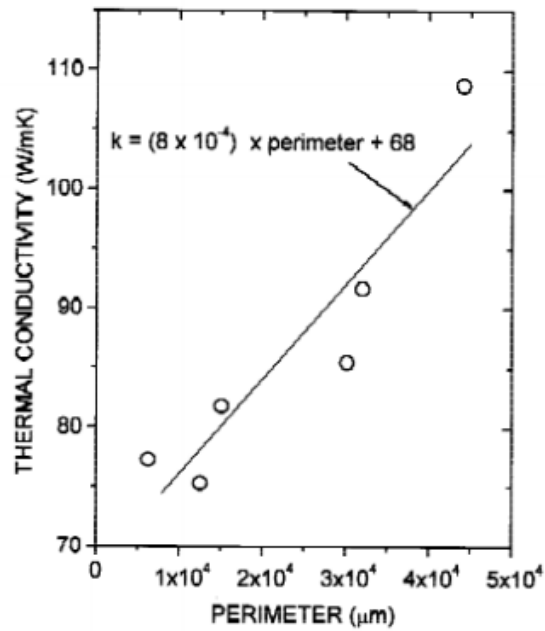


Figure 11: Dendrite perimeter vs thermal conductivity in Al A319 (Vazquez-Lopez, 1999).

Much like the effect that dendrite properties have on thermal conductivity, the dendrites also influence the electrical conductivity as well. As the cooling rate of the material increases, the electrical resistivity increases. Since conductivity is the inverse of resistivity, this means that as the cooling rate increases, the electrical conductivity decreases. This is because as the cooling rate increases the dendrite cells becomes smaller in terms of their dendrite arm spacing and overall size (Grandfield & Eskin, 2013). Figure 12 shows the relationship between cooling rate and electrical resistivity.

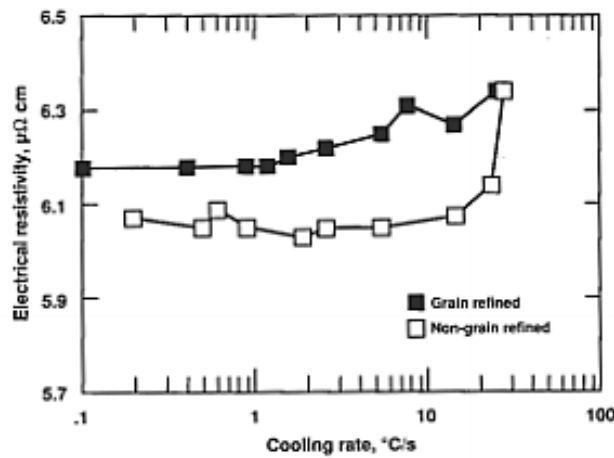


Figure 12: Cooling rate vs electrical resistivity (Grandfield & Eskin, 2013).

2.4.2 Effects of Heat Treatment and Aging Time

The research in the study performed by Hernandez-Paz in 2003 explored the effects of heat treatment on the thermal conductivity of 6061 Aluminum alloys under the T6 condition. In order to determine the effects, microhardness tests were conducted on each of the samples after heat treatment. The test was conducted by cutting and polishing samples, which were then solution treated at 543°C for 2 hours in a purified argon atmosphere and then quenched in cold water. Then the samples were aged at 163°C for various amounts of time and then quenched again before testing for micro hardness. In this experiment, the thermal conductivity was found as a product of the measured thermal diffusivity and the specific heat of the samples (Hernandez-Paz, 2003). It revealed that an increase in aging time resulted in an increase in thermal diffusivity and specific heat of the sample. Results showed a positive dependence on aging time, as shown in Figure 13.

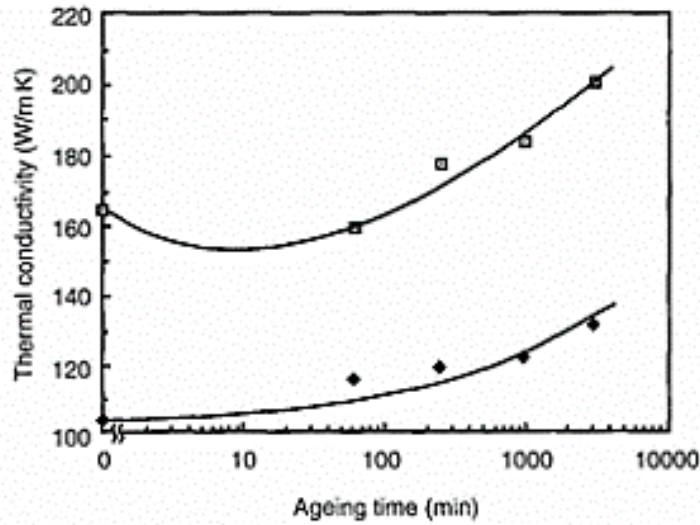


Figure 13: Aging time vs Thermal conductivity of Al 6061 (Hernandez-Paz, 2003).

In another research study, the effects of both T5 and T6 heat treatments on the mechanical properties of Al 319 were examined. Samples of a set length were solution treated and aged. Each sample was solution treated for approximately 4 hours at a temperature of 500°C and then quenched. Then the samples were aged at temperatures of 170, 200, and 220°C. After each sample was aged, Rockwell hardness tests were performed and conductivity measurements were taken using a Foster probe on the samples two flat surfaces. It was determined that the electrical conductivity of each sample reached steady state after about 4 hours of treatment. This indicates that after that point there are no more atoms in the solid solution and that the hardening mechanism is no longer effective after 4 hours (Cerri, Evangelista, Sprigarelli, Cavaliere, & DeRiccardis, 2000).

The effect of temperature on the electrical conductivity for pure aluminum, A356 and A319 cast aluminum alloys using a rotational technique was presented in another study (Bakhtiyarov et al., 2001). In this study, an apparatus was used to measure the electrical resistivity of samples at high temperature. A rheometer provided the setup with rotational speed while a thermometer within the assembly was used to measure the temperature of the samples. Figure 14 shows the variation between electrical conductivity and thermal conductivity with temperature for each of the different aluminum samples.

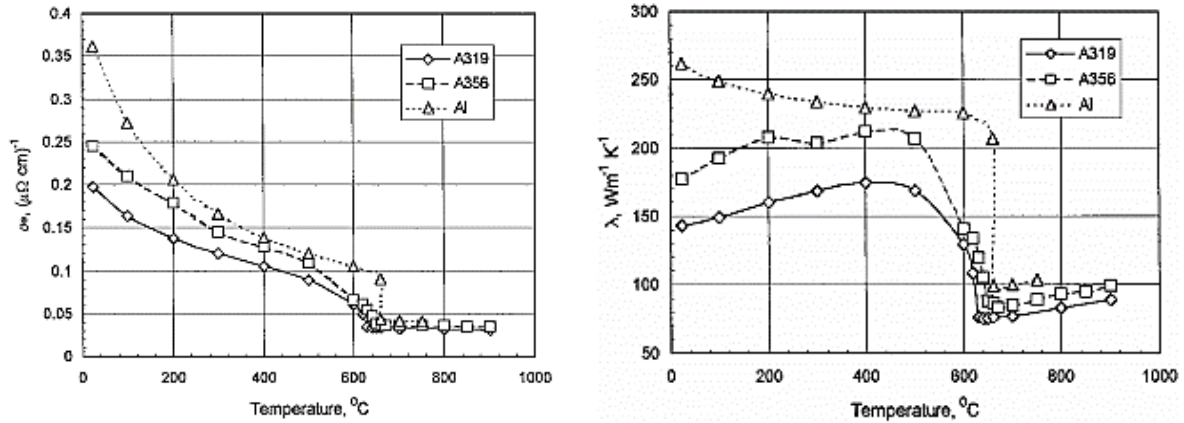


Figure 14: Variation of (left) electrical and (right) thermal conductivity with respect to temperature for pure aluminum, A319, and A356 (Bakhtiyarov et al., 2001).

Another research study was conducted to analyze the effects of heat treatment and aging on Sr-modified and unmodified A356 samples. From the experiment, it was found that the modified alloys demonstrated a high electrical conductivity in the as-cast condition than that of the unmodified sample. This is because of the movement of the electrons within the sample. Since the modified sample has a finer eutectic silicon precipitate than the unmodified sample, the electrons can flow more easily through the modified sample. Then as heat treatment is applied, a larger change in the electrical conductivity of the unmodified sample is observed. This is because of the morphology changes. A larger morphology change occurs in the unmodified eutectic silicon than in the modified which causes a larger change in its electrical conductivity (Hernandez-Paz, 2003). Figure 15 shows the electrical conductivity of modified and unmodified A356 samples.

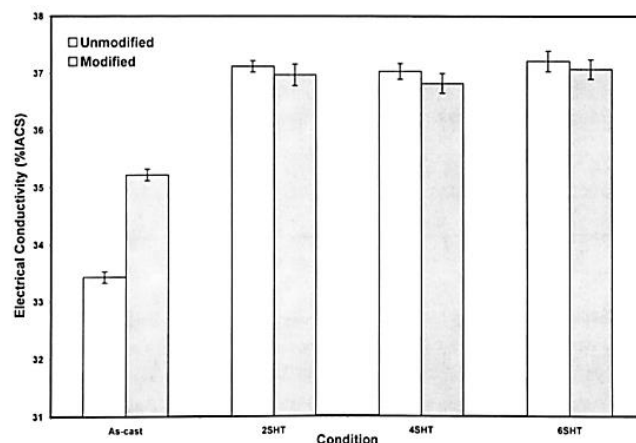


Figure 15: Electrical conductivity of modified and unmodified A356 at T4 conditions at 540°C (Hernandez-Paz, 2003).

In the following chapter the methods used for collecting the electrical and thermal transport measurements of the alloys studied will be discussed. These methods include the design and machining of the new cell, improved experimental testing procedures, and the processes used to collect and analyze data.

Chapter 3: Methodology

3.1 Sample Conditions

For the wrought alloys, we examined changes in grain orientations, aging times, and testing temperatures. Meanwhile in cast alloys, we considered the impact of grain size, dendrite arm spacing, modifications, aging times, and testing temperatures. Since there are various conditions being tested, we go on to explain in more detail the materials conditions changed for each sample in this section.

3.1.1 Cast Alloys

The cast alloys studied in this project were A356 and 319. For both alloys, we looked at variation in SDAS, Sr-modification, and heat treatment. In the A356 we also looked at variation in grain size. Tables 2 and 3 show the different conditions for A356 and 319 cast samples, respectively.

Table 2: A356 Sample Conditions

Sample				Solution Heat Treatment		Aging	
Alloy	Grain Size (um)	SDAS (um)	Modified	Time (hr)	Temperature (°C)	Time (hr)	Temperature (°C)
A356	1300	60	No	0	N/A	0	N/A
A356	1300	60	No	1.5	540	0	N/A
A356	1300	60	No	1.5	540	1.5	155
A356	1300	60	No	1.5	540	4	155
A356	1300	60	No	0.15	540	8	155
A356	1300	60	No	1.5	540	16	155
A356	1300	60	Sr	0	N/A	0	N/A
A356	1300	60	Sr	1.5	540	0	N/A
A356	1300	60	Sr	1.5	540	1.5	155
A356	1300	60	Sr	1.5	540	4	155
A356	1300	60	Sr	1.5	540	8	155
A356	1300	60	Sr	1.5	540	16	155
A356	1300	100	No	0	N/A	0	N/A
A356	1300	100	No	1.5	540	0	N/A
A356	1300	100	No	1.5	540	1.5	155
A356	1300	100	No	1.5	540	4	155
A356	1300	100	No	1.5	540	8	155
A356	1300	100	No	1.5	540	16	155
A356	500	60	No	0	N/A	0	N/A
A356	500	60	No	1.5	540	0	N/A
A356	500	60	No	1.5	540	1.5	155
A356	500	60	No	1.5	540	4	155
A356	500	60	No	1.5	540	8	155
A356	500	60	No	1.5	540	16	155
A356	500	60	Yes	0	N/A	0	N/A
A356	500	60	Yes	1.5	540	0	N/A
A356	500	60	Yes	1.5	540	1.5	155
A356	500	60	Yes	1.5	540	4	155
A356	500	60	Yes	1.5	540	8	155
A356	500	60	Yes	1.5	540	16	155
A356	500	100	No	0	N/A	0	N/A
A356	500	100	No	1.5	540	0	N/A
A356	500	100	No	1.5	540	1.5	155
A356	500	100	No	1.5	540	4	155
A356	500	100	No	1.5	540	8	155
A356	500	100	No	1.5	540	16	155
A356	500	85	Yes	0	N/A	0	N/A
A356	500	85	Yes	1.5	540	0	N/A
A356	500	85	Yes	1.5	540	1.5	155
A356	500	85	Yes	1.5	540	4	155
A356	500	85	Yes	1.5	540	8	155
A356	500	85	Yes	1.5	540	16	155

Table 3: 319 Sample Conditions

Sample			Solution Heat Treatment		Aging	
Alloy	SDAS (um)	Modified	Time (hr)	Temperature (°C)	Time (hr)	Temperature (°C)
319	60	Sr	0	N/A	0	N/A
319	60	Sr	4	495	0	N/A
319	60	Sr	4	495	1.5	180
319	60	Sr	4	495	4	180
319	60	Sr	4	495	8	180
319	60	Sr	4	495	16	180
319	85	No	0	N/A	0	N/A
319	85	No	4	495	0	N/A
319	85	No	4	495	1.5	180
319	85	No	4	495	4	180
319	85	No	4	495	8	180
319	85	No	4	495	16	180
319	85	Sr	0	N/A	0	N/A
319	85	Sr	4	495	0	N/A
319	85	Sr	4	495	1.5	180
319	85	Sr	4	495	4	180
319	85	Sr	4	495	8	180
319	85	Sr	4	495	16	180

3.1.2 Wrought Alloys

The wrought alloys studied in this project were 6061-T651 and 7075-T7351. Two samples were machined out of rolled sheets of their respective alloys. One sample was machined with its central axis parallel to the rolling direction, the other with its axis perpendicular to the rolling direction. The purpose of this is to test the effects of grain boundaries on material conductivity since the distance between grain boundaries is greater in the rolling direction.

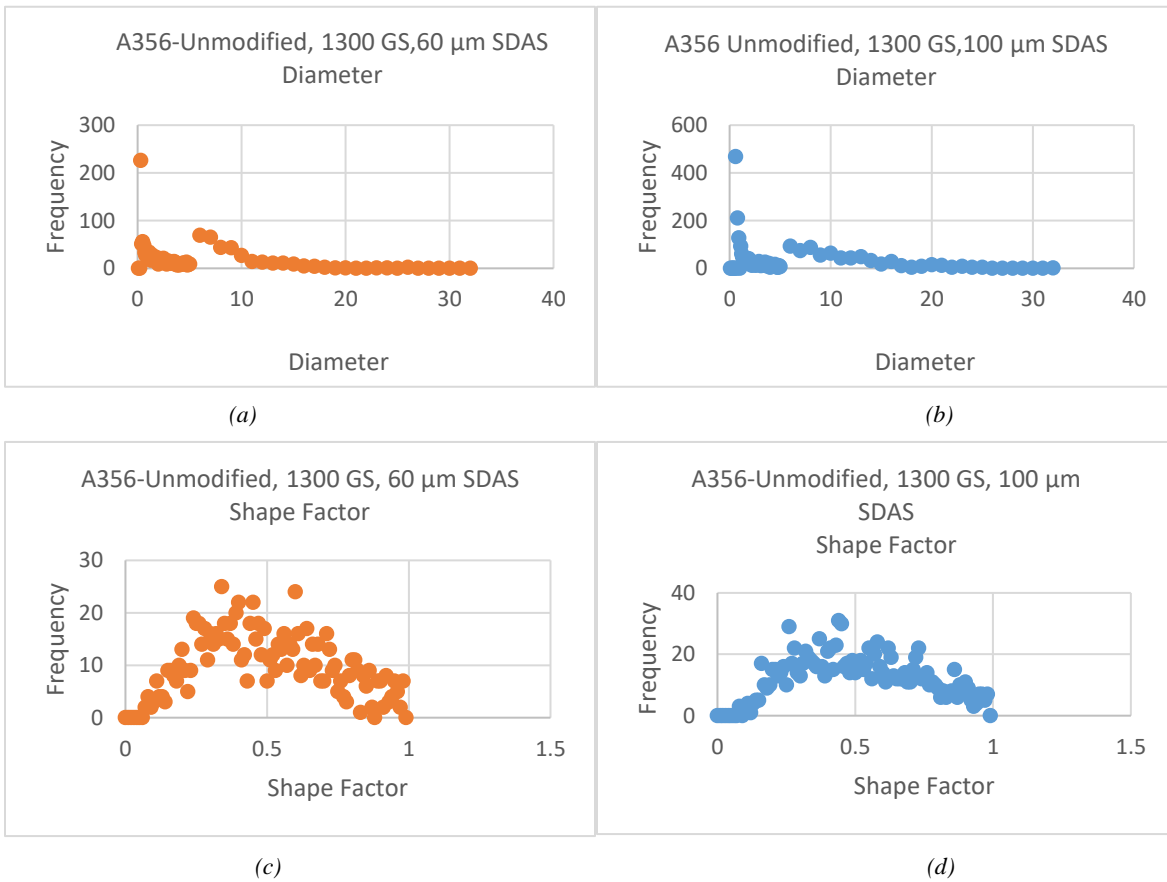
3.2 Microstructural Analysis of Test Samples & Other Properties

For each test sample, a smaller sample was created for characterizing and measuring different microstructural characteristic features. The microstructure samples were heat treated in the same way as their corresponding test sample counterparts so that there was as little variation as possible between the two samples.

Samples were mounted in phenolic pucks using a Buehler mounting press. The samples were then polished on a Buehler grinding and polishing device. The final polish was done using non-crystallizing colloidal silica suspension.

Samples were viewed using an optical microscope, and various microstructural measurements were made using image analysis software. The different measurements that were made included SDAS, and the area, equivalent diameter, aspect ratio, and shape factor of the eutectic Si particles. SDAS affects the area and equivalent diameter of eutectic Si particles, as well as the area of α -Al regions. Shape factor is a measure of surface roughness and concavity of Si particles. Additionally, microhardness measurements were made using a digital microhardness tester. The Vickers test was done with a diamond shaped indenter using a 100N force for 10 seconds.

Figure 16 shows the distribution of shape factor and equivalent diameter for select cast alloys.



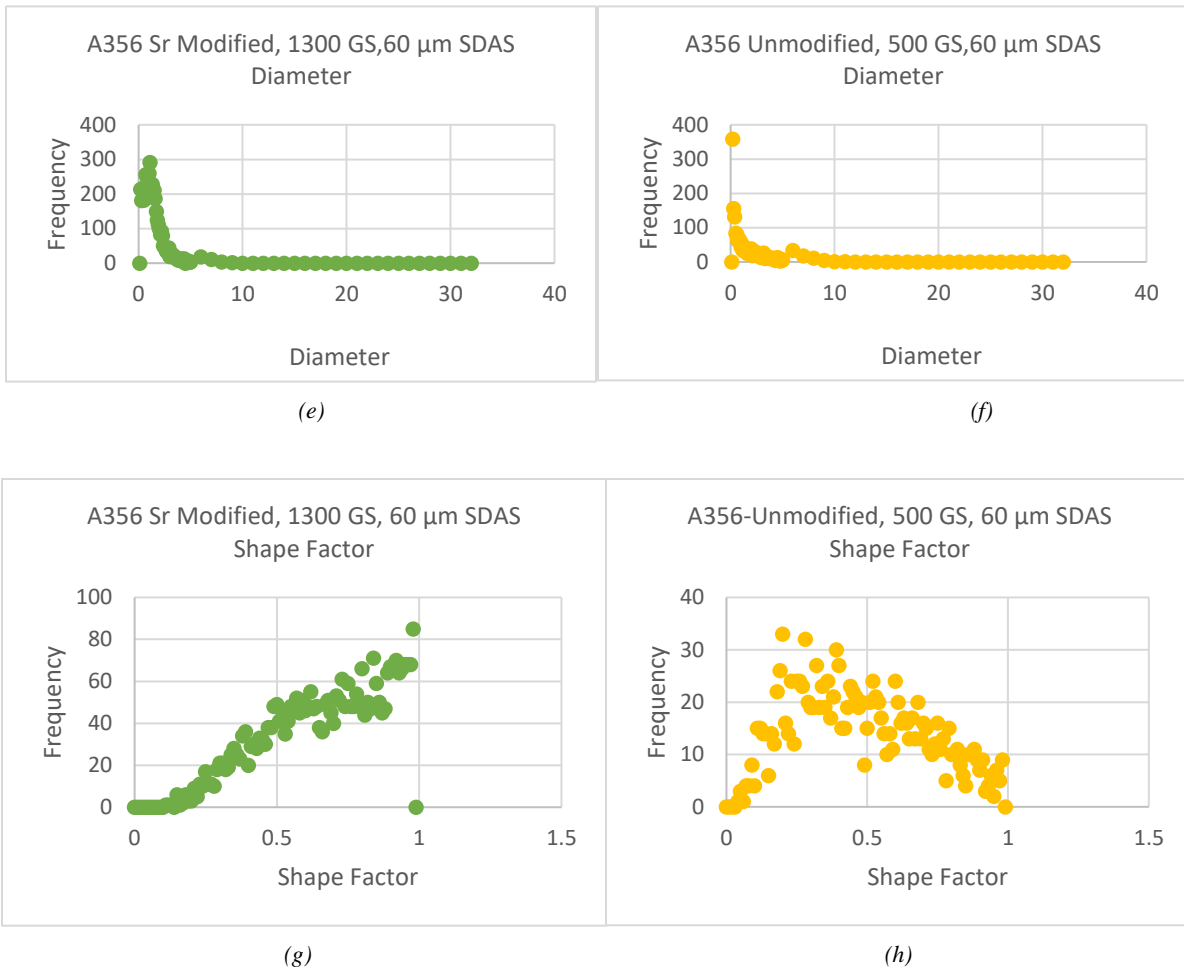


Figure 16: Distribution of equivalent diameter and shape factor of select cast alloys.

Table 4 lists information on relevant material properties of the alloys studied in this project.

Table 4: Relevant Properties of Materials Tested

Material	Density [kg/m ³]	E [GPa]	Thermal Conductivity [W/(m·K)]	Specific Heat Capacity [J/g·K]
Pure Al	2700	68.9	237	0.90
Al 356	2713	72.0	167	0.96
Al 319	2796	74.0	110	0.96
Al 6061	2700	68.9	170	0.90
Al 7075	2810	72.0	155	0.96

3.3 Cell and Specimen Design

3.3.1 Original Cell Design

The original cell, shown in Figure 17, was fabricated from polytetrafluoroethylene, also known as Teflon™ or PTFE. The original was designed to have ~1.5” of clearance from the bottom fixturing surface to the top fixturing surface, composed of a 1” diameter, 0.040” thick, copper plate. The bottom cell piece had a hole in the bottom and side of the part for electrical and heater connections to testing equipment. The top cell piece had a hole off center for electrical connections to testing equipment and also had a threaded hole for a screw to press down into the copper plate and improve the contact interface between the copper surfaces and the test sample. Both the top and the bottom pieces were attached to the body of the cell via 3 ¼-20 screws in each part, although they were not evenly spaced. Measurements of the old cell were taken to be used as a reference point to gauge the improvements of the design for the new cell.



Figure 17: Comparison between new cell design (left) and old cell design (right).

3.3.2 New Cell Design

The new cell was fabricated from Phenolic Formaldehyde, also known as Phenolic or PF. All of the new parts for the cell were prepared on a Haas Automation® Inc. TM1. The material for the cell was changed from Teflon to Phenolic in order to meet the new operating temperature requirements, since future testing will include in-situ measurements at 250°C. The new cell was

designed to have ~2" of clearance from the bottom fixturing surface to the top fixturing surface so that the cell could accommodate taller samples. The bottom cell piece, Figure 18a, still has the hole in the bottom but now also has 'steps' concentric to the original hole which were added to allow for bending of wires going from the hot copper plate to the exterior of the cell and, ultimately, the exterior of the entire apparatus. The top cell piece, Figure 18c, is still identical to the old cell. The cell body, Figure 18b, also features a shelf closer to the bottom of the cell body. All parts have an inner diameter of 1.25" and an outer diameter of 2". The cell top and bottom are each 1" tall, the cell body is 2.5" tall.

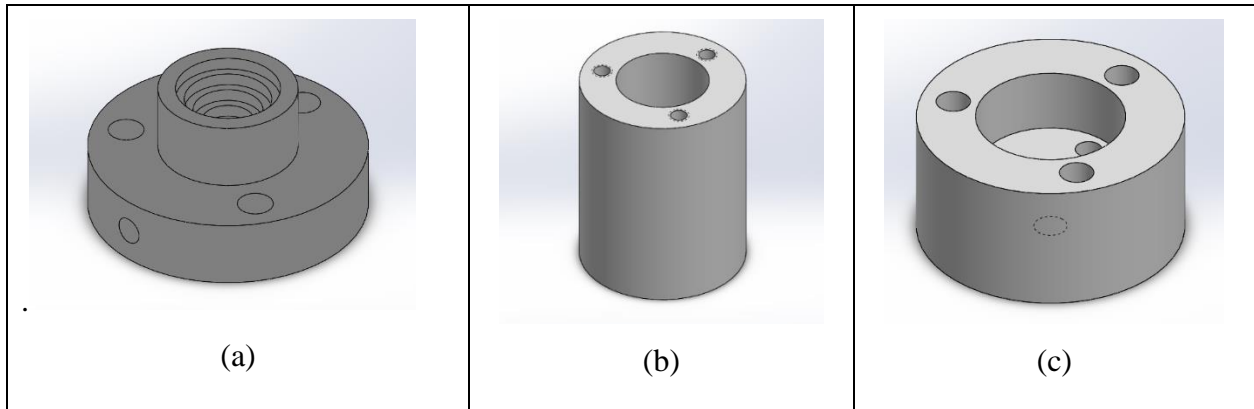


Figure 18: (a) Cell bottom (b) Cell body (c) Cell top.

The new cell design features two new parts not present in the old design, a cell sabot and a set screw cap in order to center and set the samples. See Figure 19. The sabot has a cross, the points of which are spaced ~0.4" across from the opposite point, the approximate diameter of each test specimen. The shelf in the new cell body is where the sabot rests. The set screw cap is a threaded piece that goes on the end of the set screw in the top cell piece in order to provide contact pressure with minimal contact resistance.

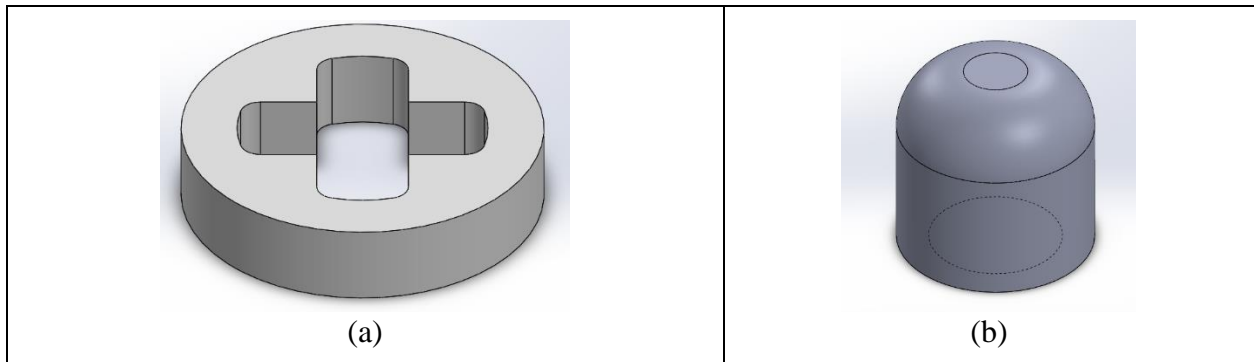


Figure 19: (a) Sample sabot: 0.25" tall, 1.25" outer diameter (b) Screw cap: 0.375" height and diameter.

3.3.3 Sample Design

Samples were made taller and thinner, shown in Figure 20 to increase the sample resistance given that resistance is proportional to length divided by area; a larger sample resistance value dominates over the instrument noise and contact resistance. Previous samples were approximately 0.6” in diameter and 1” in length, the new samples are 0.4” in diameter and 1.5” in length. This gives the new samples approximately three times the resistance of the old samples.



Figure 20: Comparison between the new sample (left) and previous sample (right).

3.4 Program Design for Thermal Measurements

Data for this project were collected using several automated programs in LabVIEW. Temperatures were measured using thermocouples read by a NI-9211 DAQmx interface from National Instruments connected via a USB port to a Windows 7 computer. The Keithley Power Supply model 2304A was computer controlled through a GPIB USB connection.

In order to optimize data collection for time, consistency, and to minimize human error, an automated program was made in LabVIEW. Figure 21 illustrates a simplified diagram explaining the automated data recording process of the LabVIEW program.

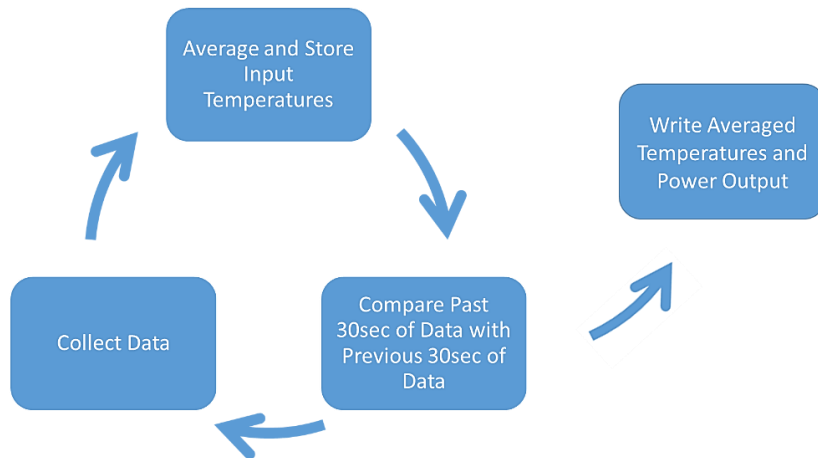


Figure 21: LabVIEW simplified flow chart.

The main section of the room temperature thermal testing program is contained within a “for loop” that repeats six times. In the beginning of the “for loop” is a stacked sequence structure as shown in Figure 22, which runs all cases in the sequence simultaneously. Each stacked sequence contains a case structure, this performs a different task depending on the input Boolean statement. For each case structure, there is an “if” statement. If the current iteration is equal to a predetermined constant, then the section of code uses the GPIB to set the voltage output of the Keithley Power Supply to a given value. The 0th iteration has an output of 0V, and therefore no power, and each subsequent iteration increases the output by 1V starting at 2V with a maximum output of 7V. These voltages correspond to dissipated power of 0.03, 0.07, 0.13, 0.20, 0.29, and 0.40W.

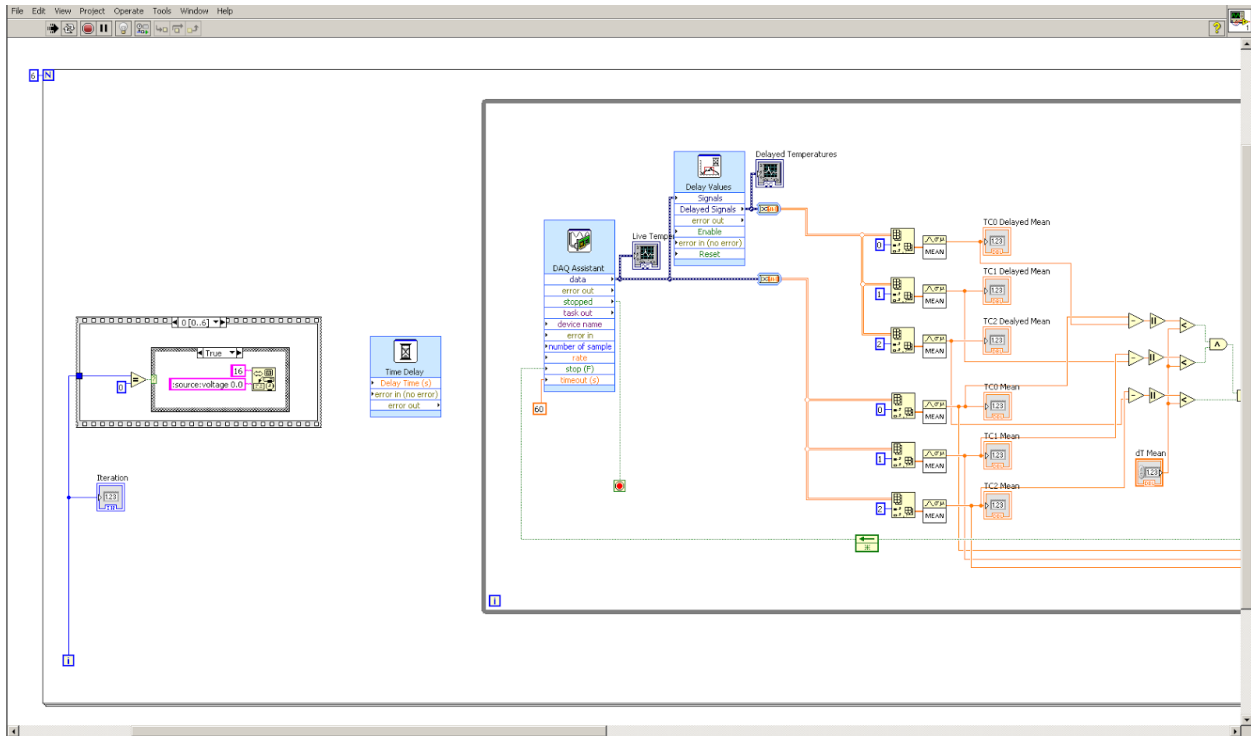


Figure 22: Beginning of For Loop containing Stacked Sequence.

After the voltage output is set, there is a two-minute delay that allows time for the temperature to respond to the new power setting before new readings begin. The program then begins a “while loop” shown in Figure 23 that collects temperature values from the three thermocouples at a rate of three readings per second for thirty seconds. The data are then duplicated, and one copy is delayed by thirty seconds. Thus, we have one 2D array containing the temperatures for the past thirty seconds, and a second 2D array containing the previous thirty

seconds of data. Each 2D array is separated into three 1D subarrays where each subarray is an individual thermocouple. The subarrays are then averaged to obtain the mean temperature for each time interval. For each thermocouple, the mean temperatures are compared between intervals. When the difference in the mean temperatures is below a specified value (typically 0.02 °C) for all three thermocouples. This indicates that the assembly has reached equilibrium and the program exits the while loop.

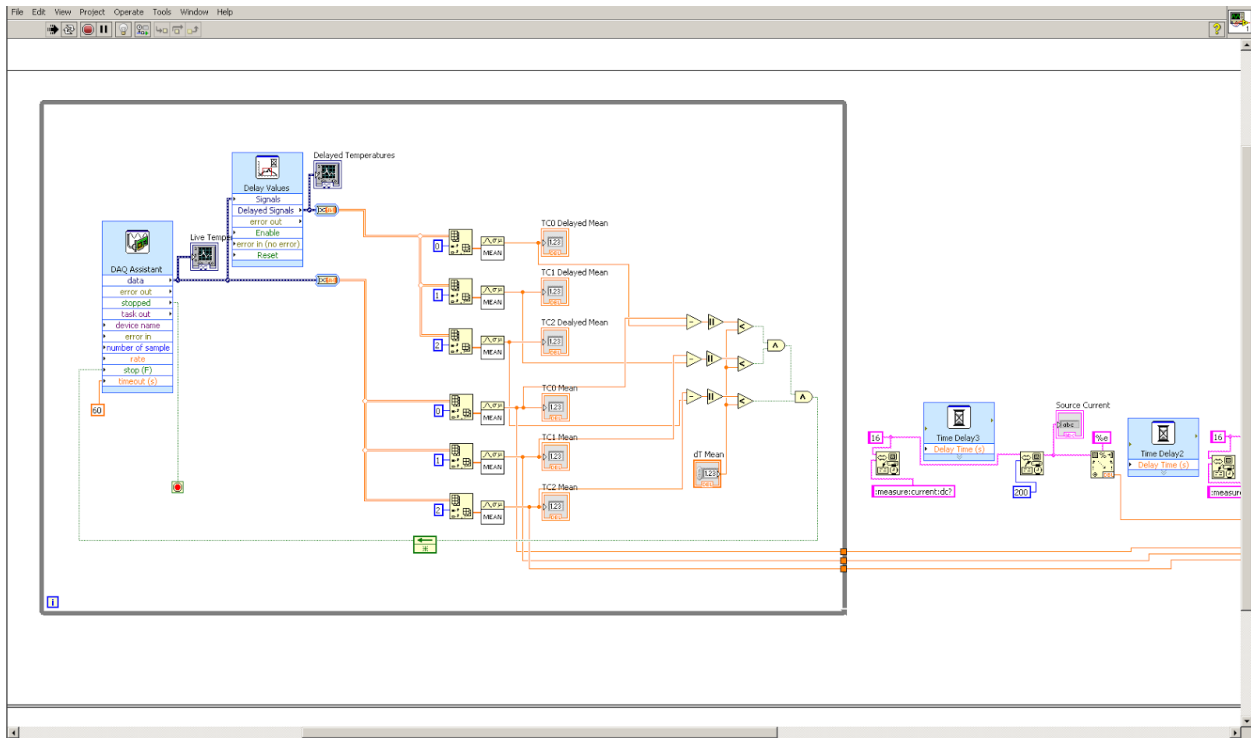


Figure 23: While Loop.

Using the GPIB, the program requests and reads the voltage and current outputs of the Keithley Power Supply and multiplies them to obtain an output power shown in Figure 24. It then writes the three average temperatures for the past thirty seconds and the output power to a previously specified text document along with the date, time, and user created comment from the front panel, see Figure 25. After completing an iteration, the program returns to the beginning of the “for loop”, increases the voltage output, and repeats the process. After the final iteration is completed the program exits the “for loop”, sets the voltage output to 0V, and the program stops.

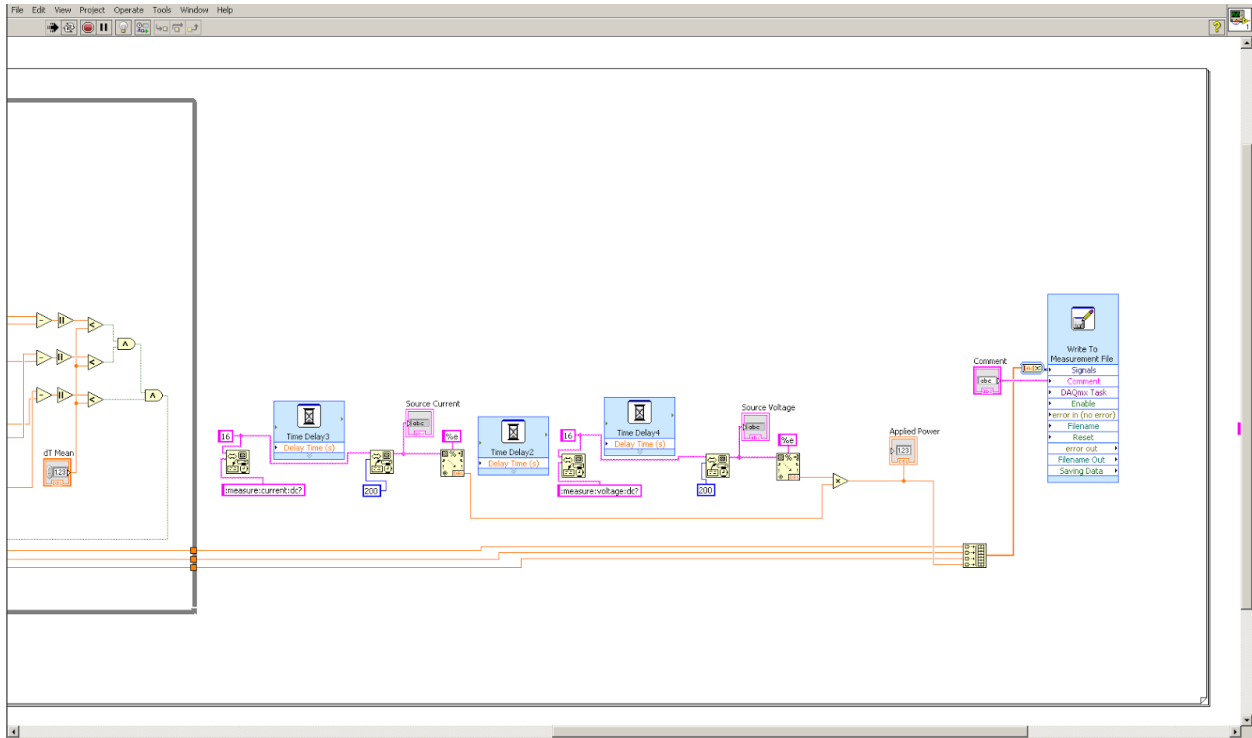


Figure 24: Reading output voltage and current.

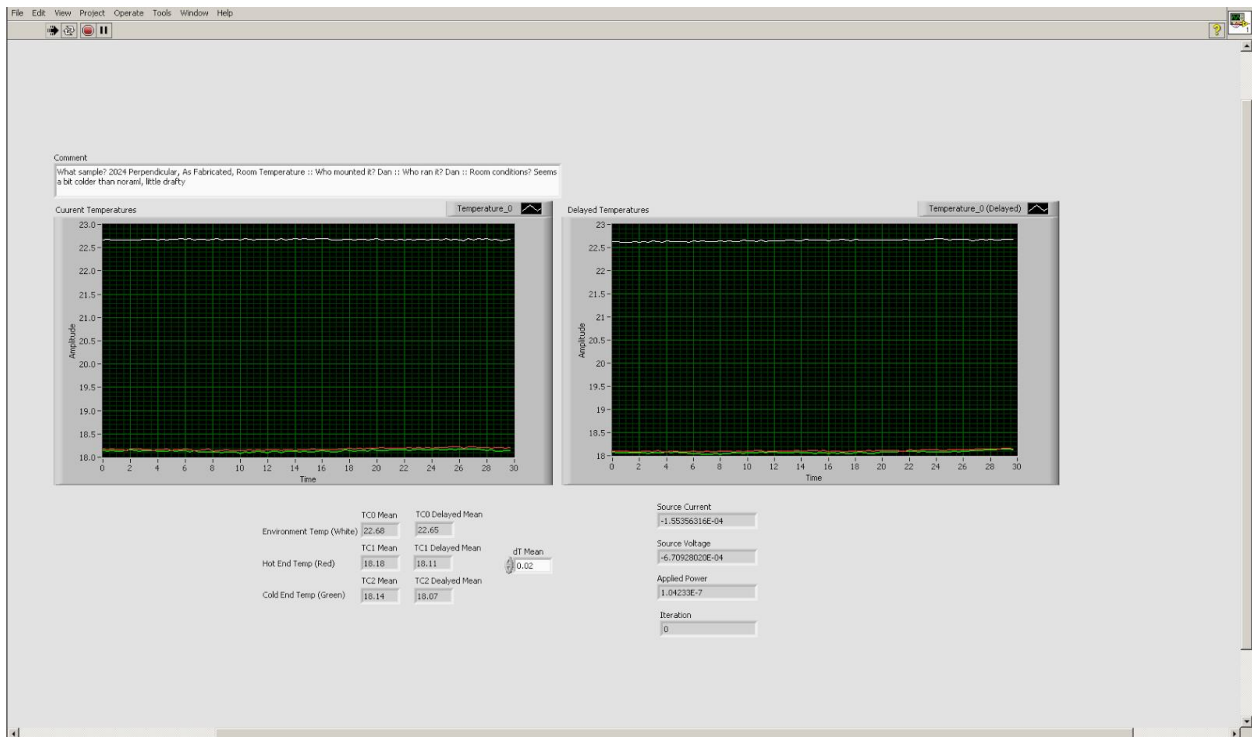


Figure 25: Front Panel.

3.5 Testing Procedure

A more in depth testing procedure manual can be found in Appendix A. The manual describes the entire testing procedure step-by-step from end polishing the samples to loading the samples in the testing apparatus and recording data for each sample. This is a brief overview of the testing procedure. Prior to measuring, the samples were labeled according to a standardized labeling system found in Appendix B.

3.5.1 Polishing Procedure

The first step in the testing procedure is to polish the samples. For the most accurate data regarding conductivity, the contact resistance between the copper plates and the ends of the test sample need to be minimized. This is accomplished by polishing the sample ends to a mirror-like finish, using a Dremel and various grit of sandpaper (ranging from 380 to 1200 grit) with a polishing solution. It is important to apply even pressure in order to keep the sample ends flat and ensure good contact with the copper plates. Once the ends have a mirror-like finish, the surfaces should not be touched in order to avoid contamination.

3.5.2 Cell Assembly Procedure

Prior to loading the polished sample into the cell, the sample's length and diameter were carefully measured in SI units using digital caliper. The sample is then placed through the sabot and into the bottom cell centering it on the bottom copper plate. The top copper plate was then placed on the top of the sample with the top cell cover attached using the three mounting screws. The center screw is then hand tightened to a consistent pressure. It is important not to over-tighten the center screw in order to avoid damaging the upper plate. The assembled cell is now lowered into the outer can, ensuring that the lead wires are wrapped around the cell, and sealed with a lid. This inner can was provided with its own thermocouple and heater to control the base temperature. This configuration was placed in an outer insulating can (dewar) and capped with a fiber-glass insulation (Fiberfrax).

3.5.3 Data-Collection Protocol

As mentioned before, a more detailed manual that gives a more in depth procedure can be found in the appendix. This is a brief overview of the procedure. Before conducting any tests refer to the Testing Procedure Manual provided in the appendix.

3.5.3.1 Thermal Measurements

To take data, the user must first get a few things set up. First, turn on the computer and open the LabVIEW program. Then, turn on the can powerstat to 5 for room temperature measurements and the Keithley 2304A High Speed Power Supply and press “Operate” to begin power output. Next, open the Block Diagram of the LabVIEW program and double click on the “Write to Measurement File” and change the file path to the desired folder and name based on the sample being tested. Finally, go back to the Front Panel of the LabVIEW program and run the program. Once the test is complete, change out the sample and begin the next test. Tests were repeated selectively in order to check reproducibility.

3.5.3.2 Electrical Measurements

Electrical measurements are made using the Keithley Model 2002 Multimeter and fixtured the sample between similar copper plates affixed with a 4-wire electrical connection. The DMM was set to “SET BY RESLN” with 8.5 digits as well as turning on the Offset Compensation. Under filtering options, the filter was set to do a repeating average of 100 data points, the output average value will update approximately every ten seconds. Twisting the sample between the plates provides alignment and ensures flatness against the copper plates. Once the sample is mounted, a wait of two minutes was imposed in order to reach a stable value, followed by manually recording six averages (over approximately one minute) and these values are averaged to yield the final measurement. The max and min values in this set is an indication of the uncertainty in the measurement. Samples were measured 4 to 6 times to verify consistency.

3.6 Transport and Heat Transfer Equations

The data collected using the procedure described earlier are then analyzed in order to extract the conductivity of the sample. Figure 26 shows a simplified diagram and model thermal circuit of the sample in the cell.

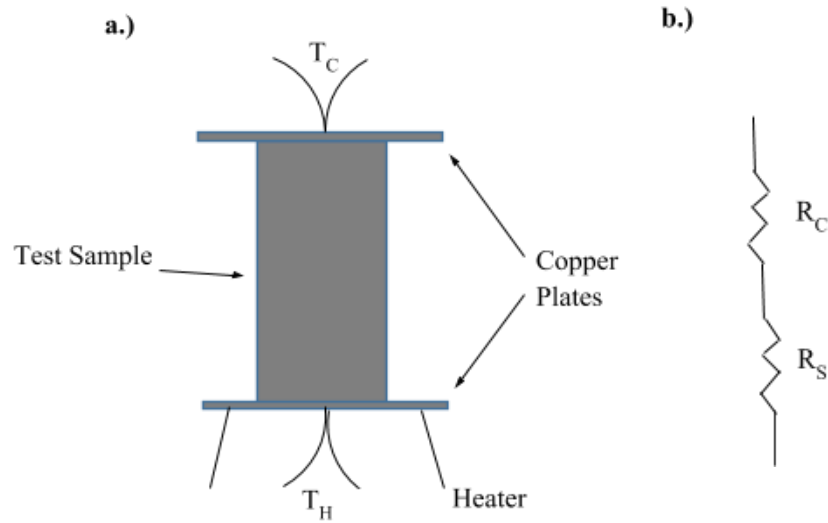


Figure 26: (a) Diagram of test sample. (b) Resistor equivalent

A calibration measurement was performed using a sample of pure aluminum having a known thermal resistance. Because the calibration sample resistance value, R_S , is known, it can be used to determine the contact resistance between the sample and the copper plates using Equations 10 and 11. Having determine R_C , the same analysis is used to calculate the R_S of an unknown sample.

Chapter 4: Results and Discussion

Having the thermal and electrical conductivity measurements for all the materials and conditions studied, a thorough quantitative analysis of the microstructures had to be done in order to create an analytical model correlating microstructural characteristics to these transport properties. The microstructural characteristics used for the correlations (for the cast alloys) include SDAS, grain size, eutectic Si particle equivalent diameter and aspect ratio, equivalent diameter and distance between eutectic Si colonies located at 3-grain junctures, and microhardness of the α -Al matrix.

4.1 Microstructural Characterization

Optical images of both cast and wrought alloys were taken, Figures 27-30, and image analysis was further performed to quantify the microstructural features used in the analytical modeling. Tables with the microstructural results can be found in Appendix C.

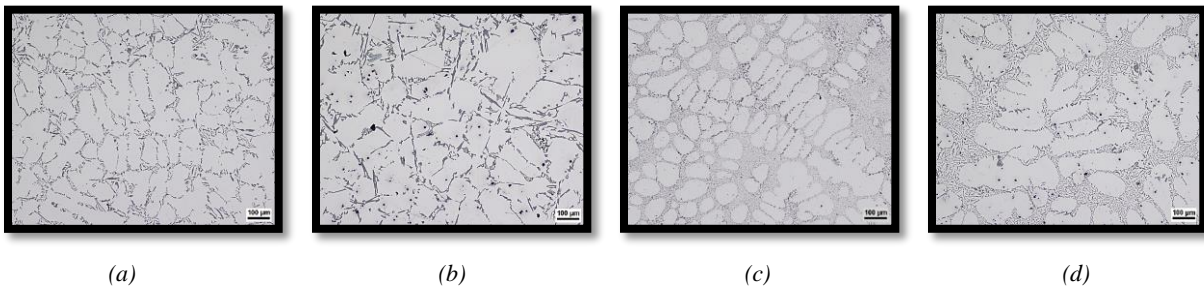


Figure 27: (a) A356-UM 500 GS 60 μ m; (b) A356-UM 500 GS 100 μ m; (c) A356+Sr 500 GS 60 μ m; (d) A356+Sr 500 GS 100 μ m.

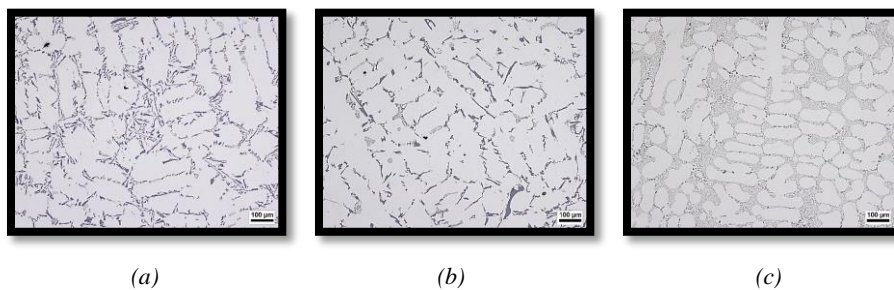


Figure 28:(a) A356-UM 1300 GS 60 μ m; (b) A356-UM 1300 GS 100 μ m; (c) A356+Sr 1300 GS 60 μ m.

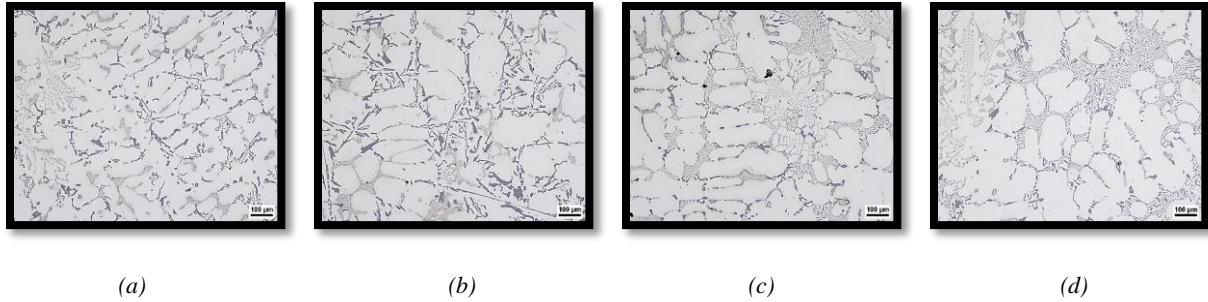


Figure 29: (a) 319-UM 500 GS 60 μm ; (b) 319-UM 500 GS 85 μm ; (c) 319+Sr 500 GS 60 μm ; (d) 319+Sr 500 GS 85 μm .

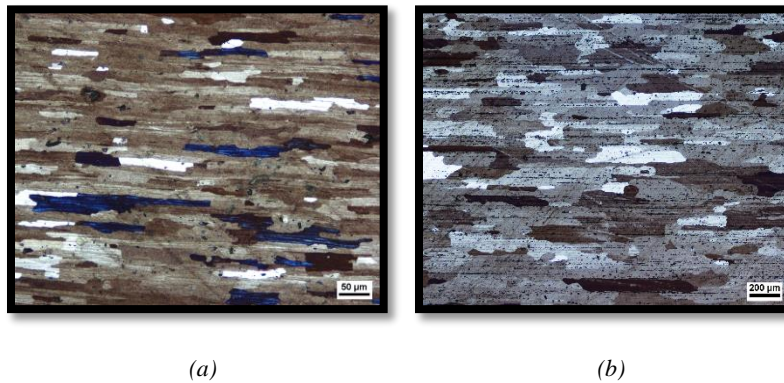


Figure 30: Etched pancake grain structure of (a) 6061 and (b) 7075.

Altering the SDAS has an effect on the area of both the α -Al regions and the eutectic Si particles. Larger dendrites obviously correspond to large regions of α -Al, but the area between dendrites also becomes larger, also having larger eutectic Si particles.

Grain size is also directly related to the area of both α -Al regions and eutectic Si particles (increasing grain size increases both). Grain size also has an impact on the distances between eutectic Si colonies, and their equivalent diameter since these colonies appear at the junctions between three grains.

Chemical modification by the addition of Sr directly alters the shape of eutectic Si within the material. Unmodified eutectic Si has a plate-like structure, while eutectic Si in the Sr-modified samples has a coral like structure in as-cast conditions. For the Sr-modified condition, the availability of the eutectic aluminum phase in the eutectic colonies is now contributing to the thermal and electrical transport, reducing the barrier effect of the eutectic Si particles.

Artificial aging (thermal modification) has a similar effect on the morphology of the eutectic Si particles as chemical modification. Eutectic Si particles first break up into smaller particles, and then begin to spheroidize and further grow with longer aging times.

The wrought alloys originate from rolled plates and have a pancake grain structure. Grains are longer in the direction of rolling than perpendicular to the rolling direction. Because of this, the distance between grain boundaries (which act as barriers to the thermal/electrical flow) depends on the orientation of the grain with respect to the measurement direction.

4.2 Thermal and Electrical Measurements

Using the methods and equations mentioned in Chapter 3, we calculated the thermal conductivity of samples with different microstructural conditions. The conductivity was then compared with variations in microstructure to determine relationship between different microstructural characteristics and conductivity.

4.2.1 Calculated Conductivities

A table of our calculated thermal and electrical conductivities can be found in Appendices D and E, respectively. Due to the large number of samples, only a select few samples were retested to gauge reproducibility. Our thermal measurements typically had an absolute precision ranging from -5 to +25%. Future tests are needed in order to confirm the absolute accuracy and repeatability of the instrument. Human error was reduced by automating the data taking process and minimizing the number of people conducting the tests. This ensured that each sample was polished and mounted as consistently as possible. For electrical measurements, the error was mostly related to the sensitivity of the DMM. Since the samples were all highly conductive, the resistance values were only slightly above the noise level. The expected resistance values were in the range of tens of micro-ohms that was approaching the limit of the resolution of the DMM. However, the general trends and differences between materials and conditions could be detected.

4.2.2 Effect of Artificial Aging Time

As samples are artificially aged, eutectic Si particles that are the primary inhibitor for thermal and electrical transport in cast alloys, begin to break down into smaller particles. The reduction in size causes them to be less of an obstacle for transport. After 1.5 hours, the eutectic Si particles begin to spheroidize and grow, changing from a low width to length aspect ratio plate-like structure to a more equiaxed shape approaching a ratio of 1. The reduction in size and more uniform shape

causes the eutectic Si particles to be less of a barrier, increasing conductivity with increasing artificial aging time. During this process, precipitates within the α -Al matrix develop and grow, but also reduce in number over time. The effects of these changes in the precipitates are overcome by the changes in eutectic Si morphology. Once the particles become spherical and isolated (between 1.5 and 4 hours of aging), there is a significant increase in conductivity, shown in Figure 31, and the aspect ratio of the eutectic Si does not change further. For aging times longer than 16 hours (overaging), the conductivity is expected to decrease as precipitates and eutectic Si particles both continue to grow.

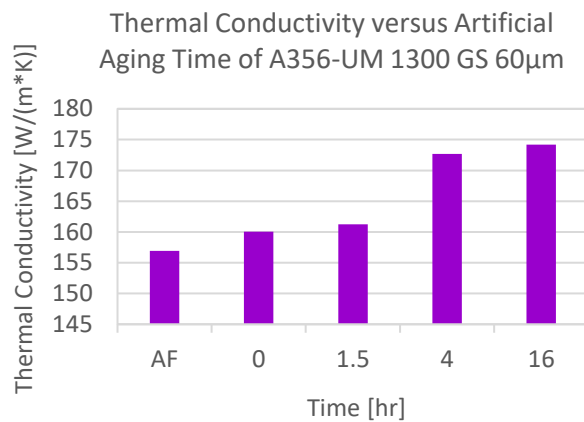


Figure 31: Thermal conductivity versus artificial aging time.

4.2.3 Effect of Sr-Modification

Chemical modification of the alloys used in this project was done with Sr. When Sr is added to these alloys it alters the plate-like growth of the eutectic Si, causing it to grow in a coral-like structure. For the Sr-modified condition, the availability of the eutectic aluminum phase within the eutectic colonies is now contributing to the thermal and electrical transport, reducing the barrier effect of the eutectic Si particles. This results in increased conductivity for the Sr-modified cases, as shown in Figure 32.

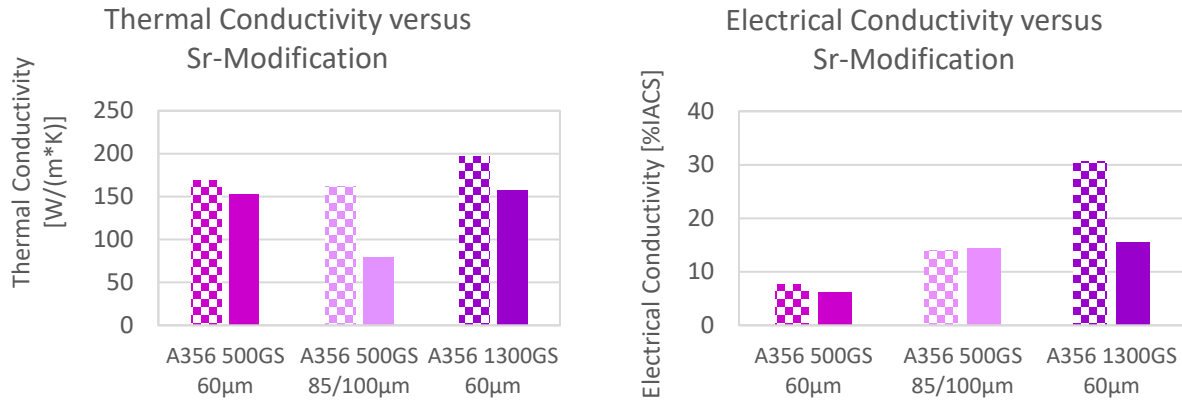


Figure 32: Chart showing effect of Sr-modification on thermal (left) and electrical (right) conductivity. Checkered represents modified, solid represents unmodified.

4.2.4 Effect of SDAS

Larger SDAS corresponds to larger α -Al regions and eutectic Si particles, however the increase in eutectic Si has a greater effect than the increase in the area of the α -Al regions. This causes thermal and electrical conductivity to decrease with increasing SDAS, as observed in Figure 33.

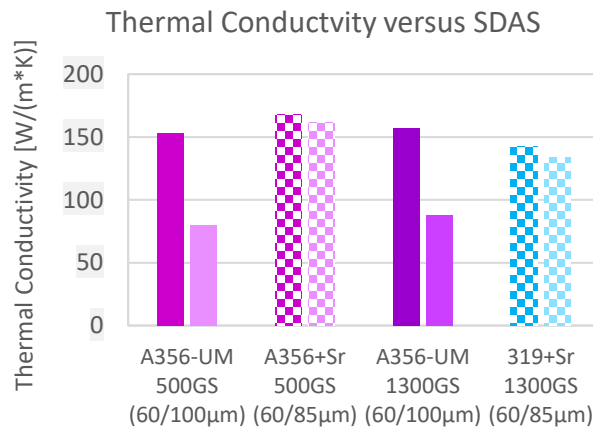


Figure 33: Thermal conductivity versus SDAS.

4.2.5 Effect of Grain Size

Increasing grain size corresponds to increasing areas of the α -Al regions, eutectic Si particles, and the equivalent diameter and distance between eutectic colonies. Grain size has a greater effect on the area of α -Al regions and the distance between eutectic colonies that occur at

the junctions of three grains. Both of these characteristics reduce the occurrence of eutectic Si particles intercepting and scattering thermal and electrical transport, and therefore, increasing grain size causes an increase in both thermal and electrical conductivities, Figure 34.

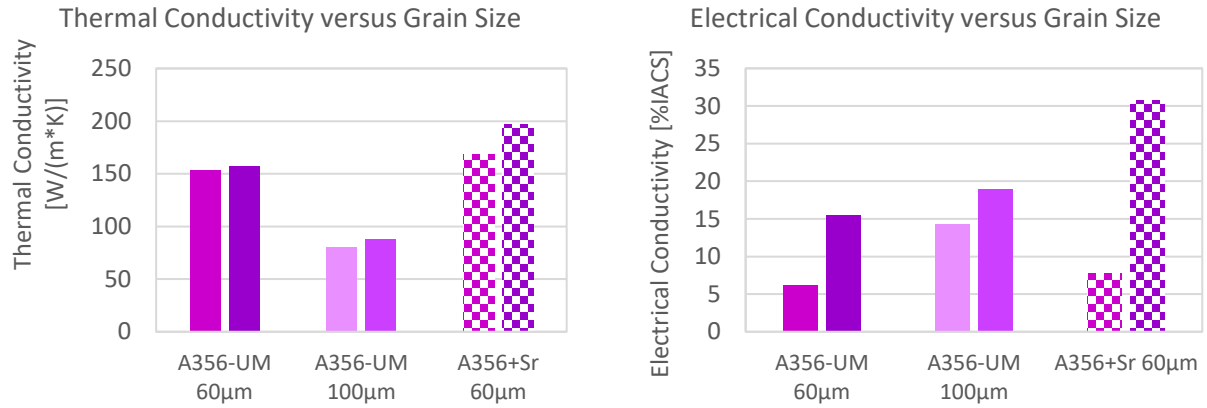


Figure 34: Thermal (left) and electrical (right) conductivity versus grain size. 500µm GS represented by the bar on the left of each cluster, 1300µm GS represented by the bar on the right of each cluster.

4.2.6 Effect of Grain Orientation

In wrought alloys, the primary inhibitor of thermal and electrical transport is scattering at grain boundaries within the material. Because of this, conductivity of a material with elongated grains is directly proportional to the grain length in the direction of the thermal or electrical flow. This is confirmed by the experimental data, Figure 35, that indicate higher conductivity parallel to the rolling direction, which is the longer grain direction.

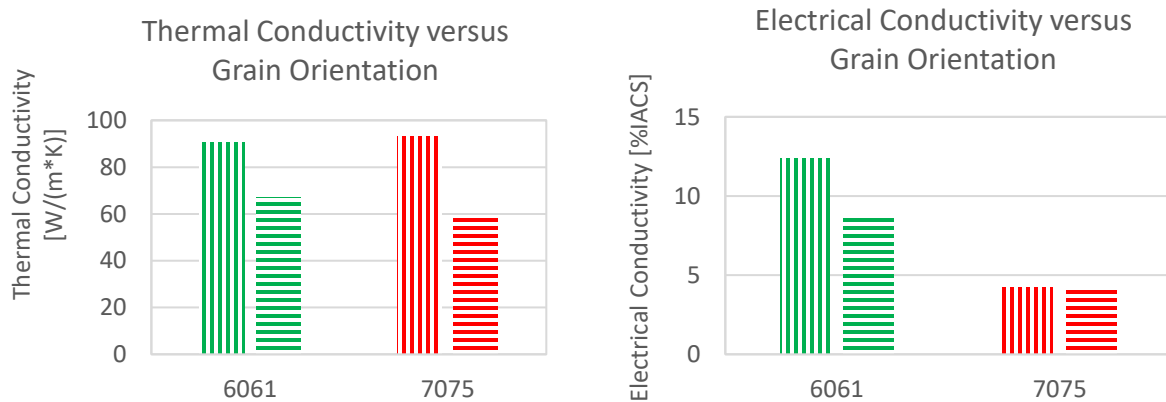


Figure 35: Thermal (left) and electrical (right) conductivity versus grain orientation of wrought alloys. Vertical stripes represent flow parallel to the rolling direction, horizontal stripes represent flow perpendicular to the rolling direction.

4.3 Analytical Model Relating Microstructure to Transport Properties

A major accomplishment in this study was the development of an analytical model correlating materials' microstructural characteristics to thermal and electrical transport properties. The reason for developing this analytical model is to allow for the prediction of the thermal conductivity of any alloy with known/similar microstructural characteristics or vice versa to select an alloy microstructure able to provide a specific conductivity.

The factors considered in this model include eutectic Si island-to-island distance and equivalent diameter, SDAS, eutectic Si particle equivalent diameter and aspect ratio, grain orientation for wrought alloys, and microhardness of the α -Al matrix, as shown in Figure 36. The data show that the eutectic Si particle equivalent diameter and aspect ratio have the greatest effect on the thermal and electrical transport properties of the tested alloys, and they both reduce the conductivity. The next most effective microstructural characteristic is SDAS, followed by grain size, and microhardness of the α -Al matrix.

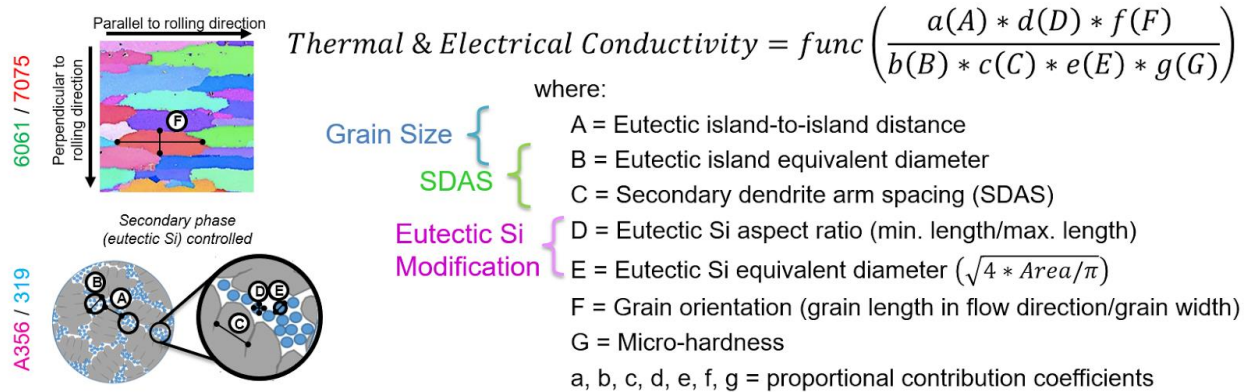


Figure 36: Analytical model equation relating conductivity to microstructural characteristics.

Chapter 5: Conclusions and Recommendations

This project incorporated the design of a custom testing apparatus to determine thermal and electrical conductivities of several cast and wrought aluminum alloys of various conditions. Microstructural characteristics were measured from the same materials used to test for conductivity. This allowed us to create a new analytical model equation which correlates microstructural characteristics to thermal and electrical conductivity, allowing us to predict conductivity of alloys with known/similar microstructures.

There are several developments that can be pursued in the continuation of this project. A major recommendation for future work is to adjust the geometry of the test samples. By making the test samples both longer and thinner, it would increase the sensitivity of the measurements taken during testing and allow for more accurate measurements. The testing methodology developed in this project can be further applied and adjusted to other aluminum and metal alloys with different microstructures and heat treatments. It would be very useful to continue developing the testing apparatus to be able to perform testing at high temperatures to allow for in-situ aging and concomitant measuring transport properties rather than perform ex-situ aging and testing at room temperature. Developing a standard polishing method (for consistently flat and mirror-like surfaces) would be helpful in reducing contact resistance during future testing. Using a thermal camera as another means of measuring the temperature differential through the sample could be another useful tool for evaluating the thermal conductivity of a sample during testing. Further enhancement to the analytical model should include development of quantitative parameters that will give weighted contributions to the controlling parameters identified in this study.

References

- Abdukadyrova, I. K., Alikulov, S. A., Akhmedzhanov, F. R., Baitelesov, S. A., Boltaboev, A. F., & Salikhbaev, U. S. (2014). High-Temperature Thermal Conductivity of SAV-1 Aluminum Alloy. *Atomic Energy*, *116*(2), 100-104. doi:10.1007/s10512-014-9825-0
- Aksöz, S., Öztürk, E., & Maraşlı, N. (2013). The measurement of thermal conductivity variation with temperature for solid materials. *Measurement*, *46*(1), 161-170. doi:<http://dx.doi.org/10.1016/j.measurement.2012.06.003>
- Bakhtiyarov, S. I., Overfelt, R. A., & Teodorescu, S. G. (2001). Electrical and thermal conductivity of A319 and A356 aluminum alloys. *Journal of Materials Science*, *36*(19), 4643-4648.
- Cerri, E., Evangelista, E., Sprigarelli, S., Cavaliere, P., & DeRiccardis, F. (2000). Effects of thermal treatments on microstructure and mechanical properties in thixocast 319 aluminum alloy. *Materials Science and Engineering*, *284*(1), 50-62.
- Collaboration for Nondestructive Testing Education. (2012). Solidification. Retrieved from <https://www.ndeed.org/EducationResources/CommunityCollege/Materials/Structure/solidification.htm>
- Davison, M. (1997). Searle's Bar (Thermal conductivity of a good conductor). Retrieved from <http://media.uws.ac.uk/~davison/labpage/searle/searle.html>
- Denisova, E. I., & Shak, A. V. (2005). Measurement of Thermal Conductivity with the IT-λ-400 Meter. In. Ekaterinburg: UGTU.
- Grandfield, J., & Eskin, D. G. (2013). Essential readings in light metals, cast shop for aluminum production. In. Hoboken, New Jersey: John Wiley & Sons, Inc.
- Harrison, T. J., Crawford, B. R., Janardhana, M., & Clark, G. (2011). Differing microstructural properties of 7075-T6 sheet and 7075-T651 extruded aluminium alloy. *Procedia Engineering*, *10*, 3117-3121.
- Hernandez-Paz, J. F. (2003). Heat Treatment and Precipitation in A356 Aluminum Alloy. In: McGill University.
- Kaufman, J. G., & Rooy, E. L. (2004). Aluminum Alloy Castings: Properties, Processes, and Applications *ASM International*.
- Key to Metals AG. (2010). Precipitation Hardening of Aluminum Alloys :: Total Matera Article. Retrieved from <http://www.totalmateria.com/page.aspx?ID=CheckArticle&LN=EN&site=ktn&NM=235>
- Mahanta, N. K., & Abramson, A. R. (2010). The dual-mode heat flow meter technique: A versatile method for characterizing thermal conductivity. *International Journal of Heat and Mass Transfer*, *53*(23-24), 5581-5586.

- Majumder, P., & Bhattacharyya, A. (2008). A computational study on the impact of the Wiedemann-Franz-Lorenz Law on the thermal response of nichrome cylinders. *Modeling and Simulating in Material Science and Engineering*, 16(1).
- MatWeb. (2016). MatWeb Material Property Data.
- Nave, C. R. (1998). Resistance and resistivity. In.
- Nielsen (ed.), H. (1979). *Handbook of Aluminum Alloys: Properties, Machining, Applications [Russian translation]*. Moscow.
- Pace Technologies. (2014). Introduction to Metallurgy. Retrieved from <http://www.metallographic.com/Technical/Metallography-Intro.html>
- Starke, E. A., & Staley, J. T. (1996). Application of modern aluminum alloys to aircraft. *Progress in Aerospace Sciences*, 32(2), 131-172. doi:[http://dx.doi.org/10.1016/0376-0421\(95\)00004-6](http://dx.doi.org/10.1016/0376-0421(95)00004-6)
- TA Instruments. (2012). Principle methods of thermal conductivity measurements. In.
- The Aluminum Association. (2015). International Alloy Designations and Chemical Composition Limits for Wrought Aluminum and Wrought Aluminum Alloys. In: The Aluminum Association, Inc.
- Toozandehjani, M., Mustapha, F., Zahari, N. I., Ariffin, M. K. A., Matori, K. A., Ostovan, F., & Lim, W. F. (2015). Characterization of Aging Behavior of AA6061 Aluminum Alloy Through Destructive and Ultrasonic Non-destructive Testing Techniques. *Transactions of the Indian Institute of Metals*, 68(4), 561-569.
- Ushie, P., Osang, J., Ojar, J., Daniel, T., Ettah, E., & Alozie, S. (2014). Determination of thermal conductivity of some materials using Searle's Bar and Ingen Housz experimental methods. *Journal of Current Research in Science*, 1(2), 63-66.
- Vazquez-Lopez, C. (1999). Influence of dendrite arm spacing on the thermal conductivity of an aluminum-silicon casting alloy. *Journal of Materials Research*.
- Woodcraft, A. L. (2005). Predicting the thermal conductivities of aluminum alloys in the cryogenic to room temperature range. *Cryogenics*, 45(6), 421-431.
- Xing, C., Jensen, C., Ban, H., & Phillips, J. (2011). Uncertainty analysis on the design of thermal conductivity measurement by a guarded cut-bar technique. *Measurement and Science Technology*, 22(7).
- Zajas, J., & Heiselberg, P. (2013). Determination of the local thermal conductivity of functionally graded materials by a laser flash method. *International Journal of Heat and Mass Transfer*, 60, 542-548.

Appendix A: Procedure Guide

This document contains instructions on how to prepare the samples for testing, and detailed notes on how to collect thermal and electrical measurements for this project.

Table of Content

Cell Assembly.....	50
Loading Test Sample.....	53
Making & Recording Thermal Measurements.....	57
Making & Recording Electrical Measurements.....	60
Notes for Disassembly of Cell.....	60
Making & Recording Electrical Measurements.....	61
Notes for Disassembly of Cell.....	61
Polishing Procedures.....	62
Polishing Test Samples.....	62
Polishing Microstructure Samples.....	63

Cell Assembly

Two identical cells were machined out of phenolic formaldehyde for this project, one for thermal experiments, and the other for the electrical experiments. The cell is composed of various parts including the top, bottom, body, sabot, and one inch pure copper polished disk; the sabot is used to keep the sample in place. Figure 1a and 1b show the cell components, and Figure 2 shows the copper plates.

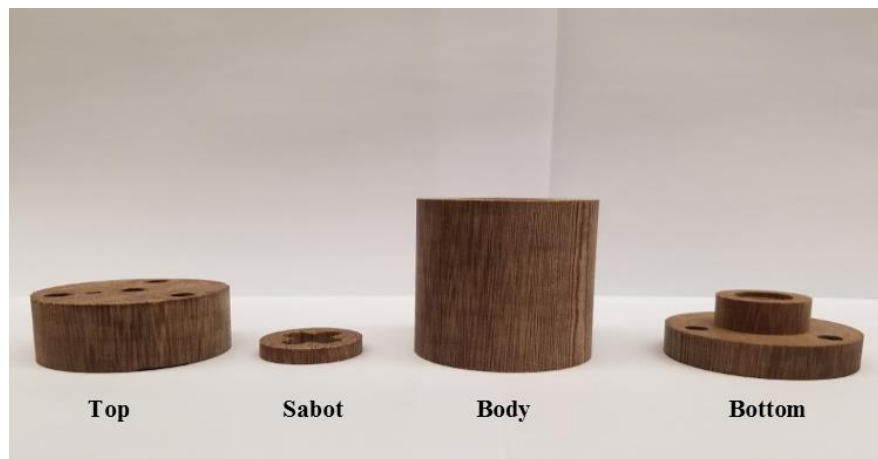


Figure 1a: Cell Components.

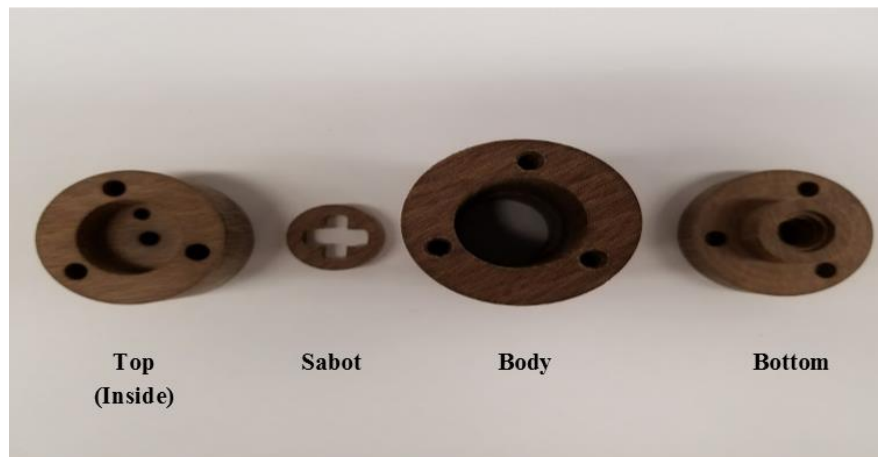


Figure 1b: Top view of cell components.



Figure 2: Polished copper disks.

Six steel $\frac{1}{4}$ "-20 screws were used to tighten the cell close (see Figure 3). An additional $\frac{1}{4}$ "-20 2 inch long phillips aluminum screw was used to make the final connection to the test sample, since it was longer.



Figure 3: Screws used to tighten cell close.

- Carefully place bottom copper plate on the bottom base (see Figure 4).

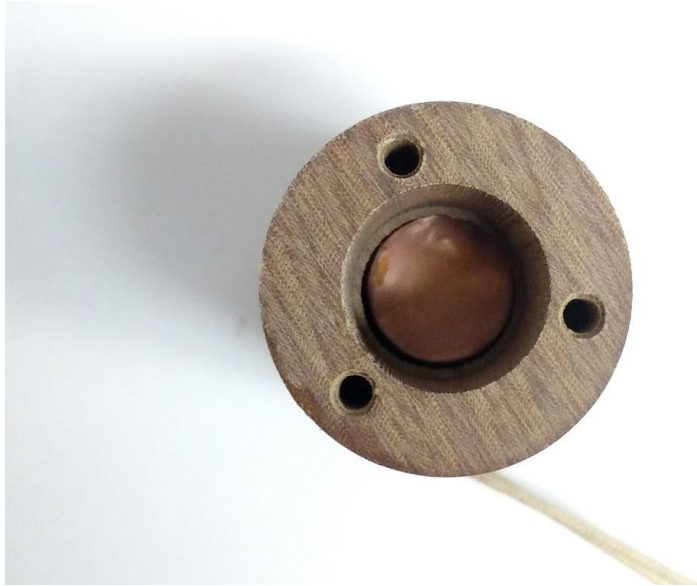


Figure 4: Copper plate on bottom base.

- Screw the bottom base to the body of the cell with the steel screws (through the bottom of the cell in Figure 4).

Loading Test Sample

- Prior to loading the sample measure the length and diameter of the sample in SI units! (mm). Record this in the “Measurements and Calculations” file in the “Matrices & Calculations” Folder.
 - To find this folder go to:
Google Drive->Materials Transport MQP 2016-2017->Matrices & Calculations->Measurements and Calculations.xlsx
- Place test sample through the sabot and center it against the copper plate as best as possible.
- Place the polished side of the top copper plate on the top end of the sample. Ensure the copper plate is touching the entire surface area of the test sample.
- Use the allen key to tighten the three screws on the outer diameter of the cell’s cover. Tighten until slight resistance is felt. These screws do not need to be very tight, they do not carry any tension of the cell.
- Hand tighten the center screw located on the top of the cell. The screw should be tightened until moderate resistance is felt against the screw.
- Carefully lower the cell into the can.
 - Make sure there is enough extra cable and wire to move cell with ease from the work table into the can and vice versa.
 - When placing the cell into the can wrap some of the wire around the side of the cell.
 - NOTE: Make sure that as you are lowering the cell, none of the wires get caught on anything on the table such as the screws mounting the can. Any caught wire may get pulled out or broken.
- Make sure some of the wire touches the side of the can, around the cell (see Figure 5).
 - This helps dampen the fluctuation of temperature from the outside environment.

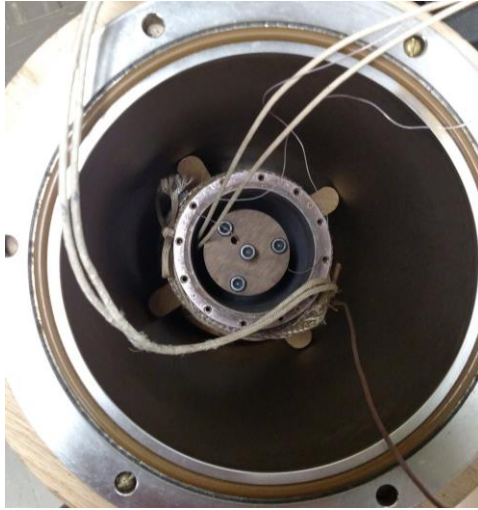


Figure 5: Cell in can with wires wrapped around.

- Carefully place the collar into the can, covering the cell, (See Figure 6a.)
 - First pull the slack in the wires, then place collar. Finally, add wire back into the cell so that it touches the base.
 - Make sure the collar DOES NOT pinch any of the wires.
 - NEVER set the collar flat on the table, ALWAYS lay the collar on its side.

- Use two to four screws to lock the collar in place. Tighten the collar using mild tension; these do not need to be very tight. This is only to create a seal and prevent the collar from shifting.

- Use the stopper (steel wool for now) to close up hole in the top of the collar (see Figure 6b).

- Place insulation inside the can (Figure 7).

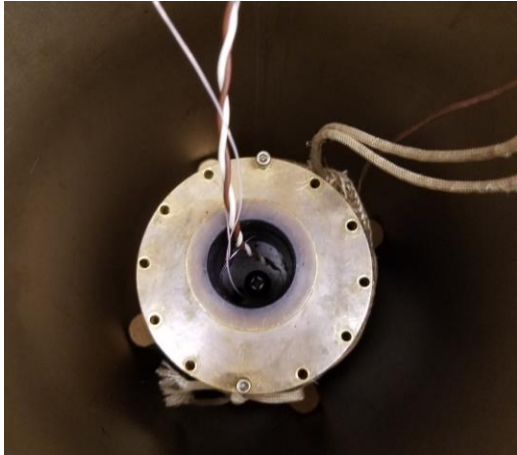


Figure 6a: Collar.

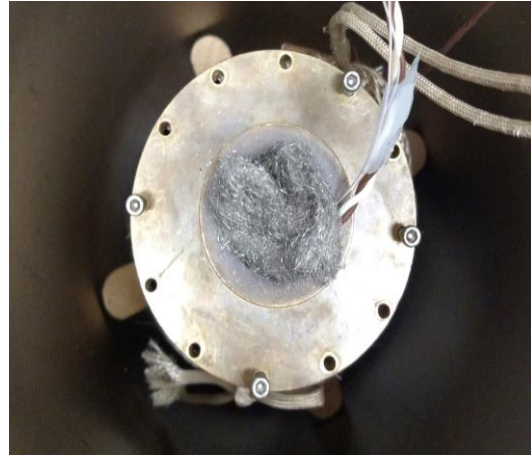


Figure 6b: Stopper in collar.

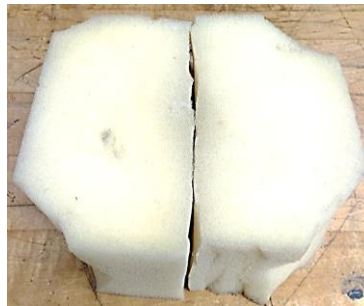


Figure 7: Insulation.

- Cover can with wooden cover, add weights on top if needed.
 - Make sure that the screws in the cover line up with the holes in the can and that no wires are pinched between the two halves of the cover.



Figure 8: Wood cover.

Making & Recording Thermal Measurements

After the sample has been measured and loaded according to the loading sample procedure follow the steps below to record thermal measurements.

- Turn on pc, open LabVIEW, run project file “Automated Thermal Data Collection - Transport MQP”, off of desktop.

- Open Measurements and Calculations excel file from Google drive.
Google Drive->Materials Transport MQP 2016-2017->Matrices & Calculations->Measurements and Calculations.xlsx

- Turn on the can POWERSTAT (Figure 9a and 9b)
 - For measurements at room temperature set the POWERSTAT to 5.
 - For measurements in situ set the POWERSTAT to 45.
 - The can takes a very long time to heat up, even to 25 degrees, it is recommended that you turn the POWERSTAT to a higher setting and reduce it when you get close to the target temperature.

- Turn on the Keithley 2304A High Power Supply (see Figure 10).
 - Press the power button.
 - Wait for display to clear.
 - Press “OPERATE”. This will begin power output to the bottom copper plate of the cell.
 - ✓ You will know the power is being output by looking at the top right row on the display. It will show “ON” or “OFF”

- Open the Block Diagram of the LabVIEW file (you do this by pressing ctrl+E while looking at the Front Panel).

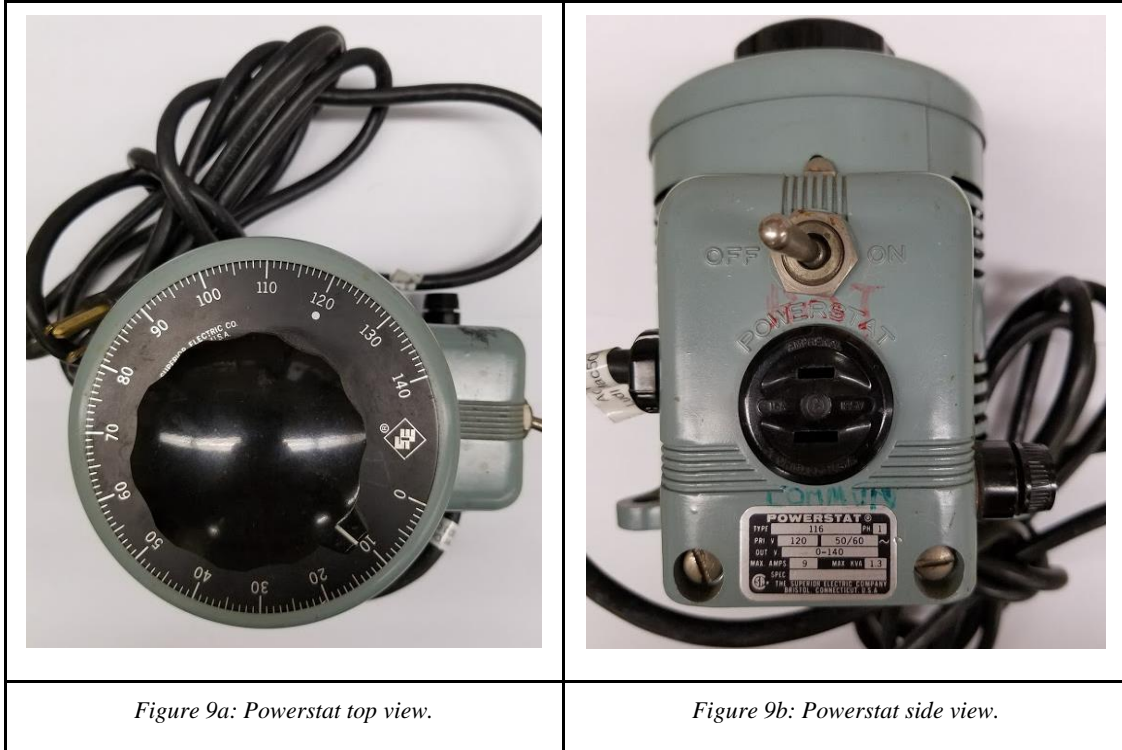


Figure 9a: Powerstat top view.

Figure 9b: Powerstat side view.

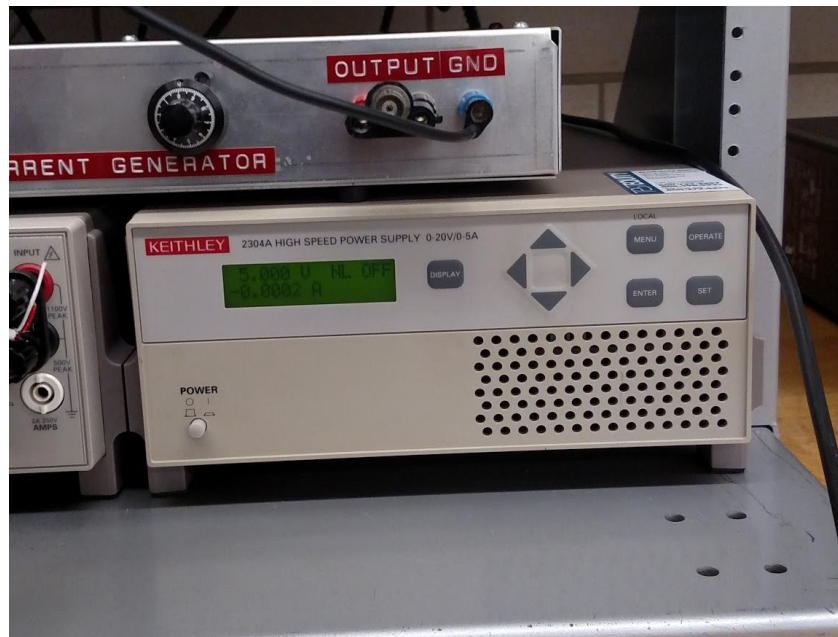


Figure 10: Keithley 2304A High Power Supply.

- Double click on the “Write to Measurement File” subVI (this will open the options for the subVI) (see Figure 11).

- Change the file path to the appropriate folder and name based on the file naming conventions and click OK (see Figure 12).

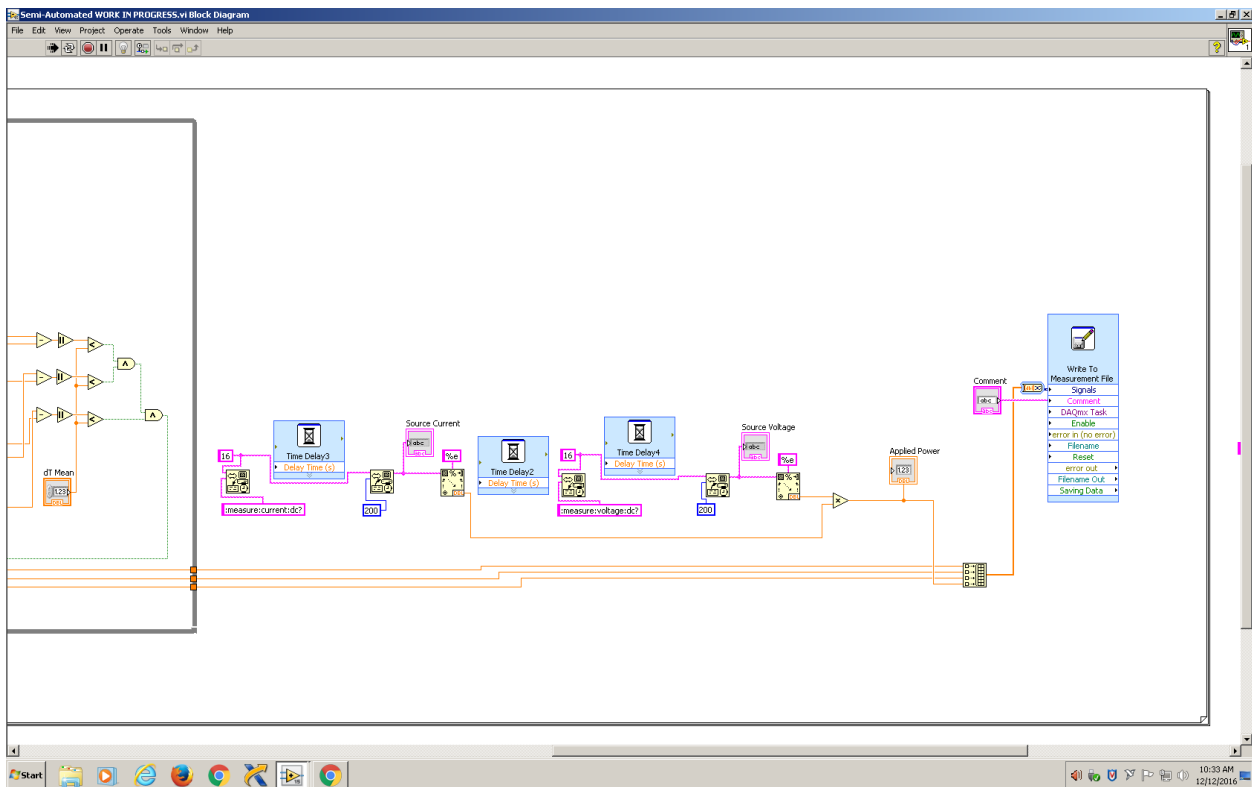


Figure 11: Write to Measurement File subVI in LabView Block Diagram.

- Go back to the Front Panel and run the program (to do this, click on the white arrow in the top left, below “File”) (see Figure 13).
 - The program should now automatically run through 0, 0.5, 1.0, 1.5, 2.0, 2.5, and 3V outputs

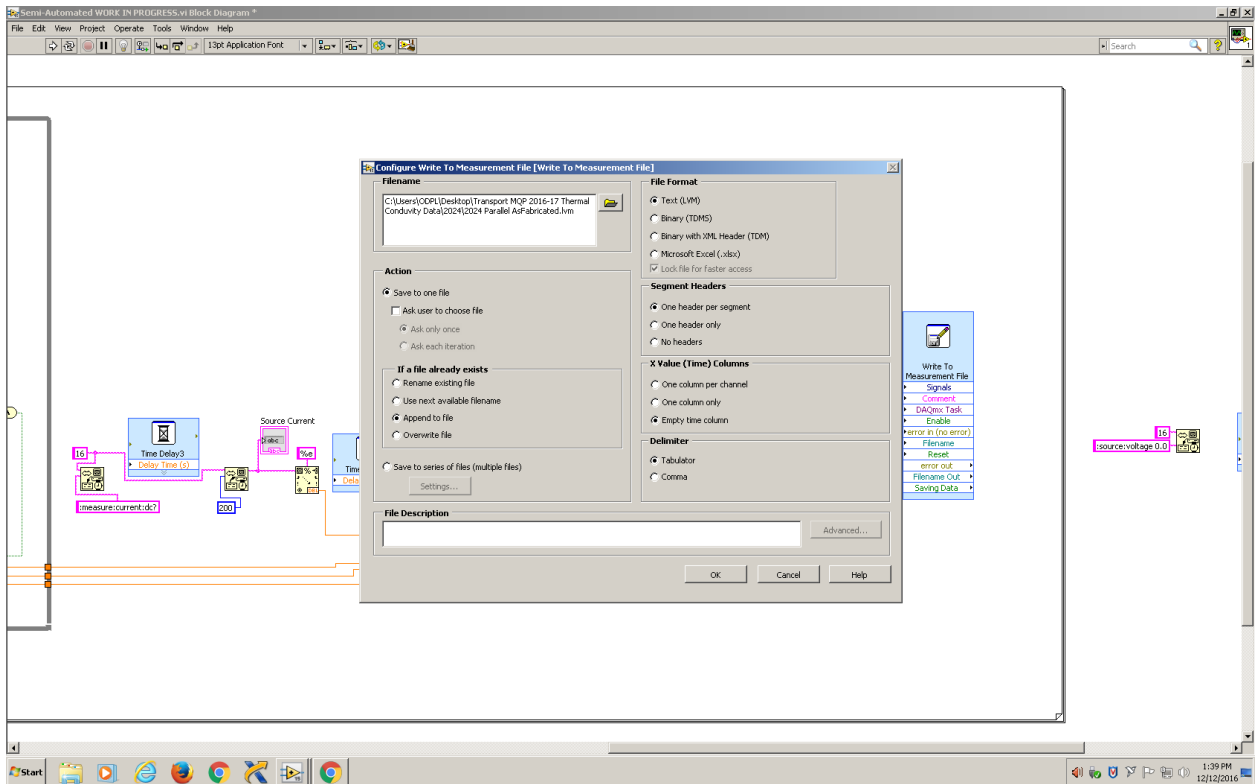


Figure 12: Write to Measurement File Options.

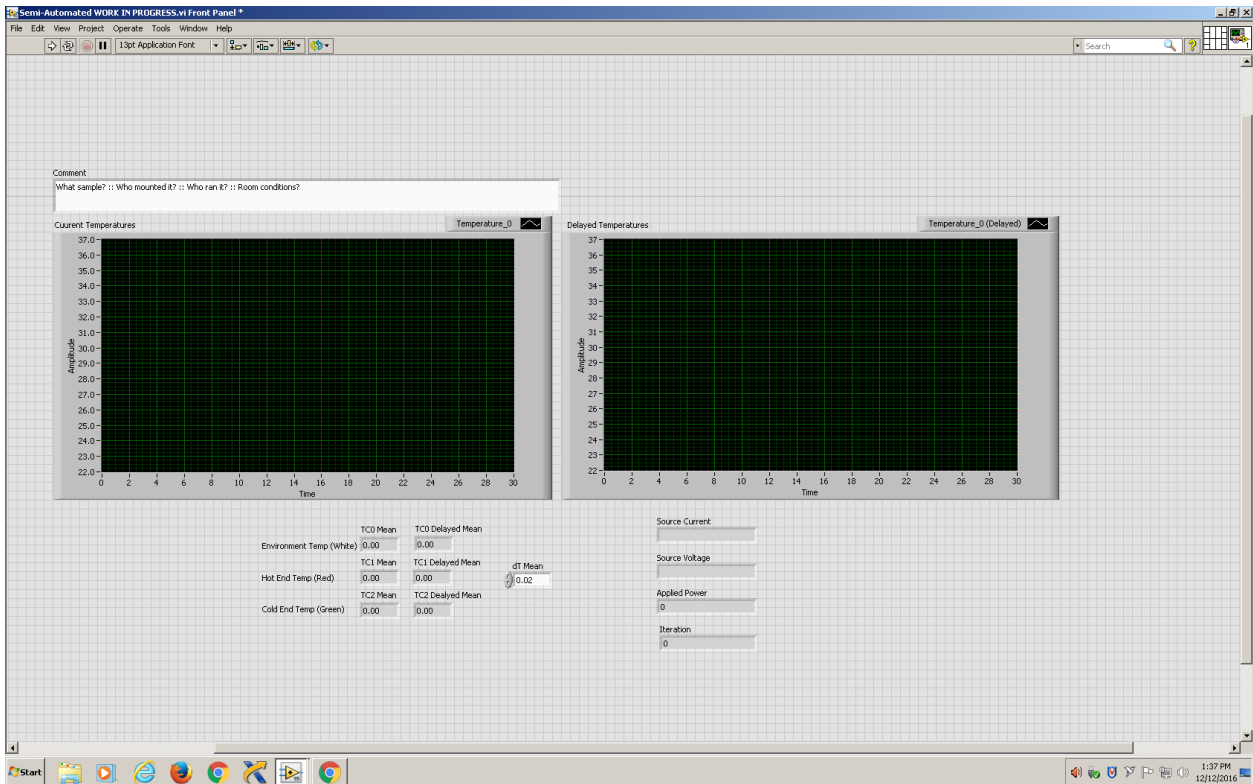


Figure 13: LabView Front Panel.

Making & Recording Electrical Measurements

Electrical measurements are made using the Keithley Model 2002 Multimeter. Set the multimeter to “SET BY RESLN” and set it to 8.5, then turn on the Offset Compensation. Under filtering options, set the filter to do a repeating average of 100 data points, the average will update approximately every ten seconds. The sample is placed into the vice between the two copper plates. Twist the sample to align it so that the contact ends are flat against the copper plates. Wait two minutes for the sample to reach steady state, then manually record six averages (approximately one minute) and average those values for one test. Repeat 4-6 tests for consistency.

Notes for Disassembly of Cell

- Never cause tension on the wires
- Always lay the collar on its side to avoid crimping the wires
- Use center screw to lift the cell out of the can
- After removing cell out of can loosen center screw first, then unscrew outer screws

Polishing Procedures

Polishing Test Samples

The purpose of polishing the sample is to provide the best surface for testing. The desired surface should be perfectly flat and provide a “mirror-like” image. Polish sample using the appropriate polishing technique. After the samples have been polished, consider using gloves to prevent contamination.

*****Do not touch the ends of the samples once polished, it will contaminate them!*****

STEP 1: Attach 380 grit sandpaper on the Dremel.

STEP 2: Press edge of sandpaper on the Dremel against the ends of the test sample using a small circular motion.

STEP 3: Apply equal pressure throughout the surface area in order to maintain a flat surface on the end of the sample.

STEP 4: Once the surface appears clean, and clear of any imperfections, place the sample vertically against a flat surface (i.e the work table). This is to ensure the end of the sample is still flat. If not, Dremel the sample as needed to obtain the flat surface.

STEP 5: Switch the sandpaper on the Dremel to 600 grit sandpaper and repeat STEPS 2-4.

STEP 6: use 2 or 3 drops of Buehler Metadi (see Figure 2) solution on the end of the samples.

STEP 7: Switch the sandpaper on the Dremel to 1200 grit and repeat STEPS 2-4 until a mirror like flat surface is obtained.

STEP 8: Once satisfied with the polishing of the sample, clean off any residue on the ends with a paper towel.

Polishing Samples for Microstructural Characterization



Figure 14: Buehler Metadi Polishing. Solution

To perform microstructure analyses of each test sample, a small piece of each material was cut, and polished using the AUTOMET 250 Polisher (see Figure 15). This machine prepares the specimens for metallographic work. Prior to mounting the microstructure samples to the machine, the samples need to be molded into a phenolic puck. Follow the instructions posted next to the machine in the laboratory. An image containing the complete set of instructions can be seen in Figure 16.



Figure 15: AUTOMET 250 Polisher/Grinder.




There are two types of polishing procedures based on the copper content of the test samples. For alloys with low copper content, the team used a colloidal silica solution (see Figure 17). For alloys with relatively high contents of copper, we used a diamond solution, since the colloidal silica etched the copper. Table A contains the steps for polishing samples with colloidal silica.

For the AUTOMET 250 settings that remained unchanged throughout the polishing were:

Load on Specimen- 20 [N]

Head Speed-60 [RPM]

Table A: Polishing Aluminum alloys in the AUTOMET 250 using colloidal silica.

Step #	Sand Paper Grid	Base Speed [RPM]	Relative Rotation	Time [Minutes]	Notes
1	320	300		3	Set water "state" to OFF & "step active" to ON.
2	600	300		3	Set water "state" to OFF & "step active" to OFF.
3	Polishing Disc	150		20	-Set water "state" to OFF & "step active" to OFF. -Add colloidal silica solution every 30 seconds. -Add water every 2 minutes (prevents silica from solidifying).

Where:  = Platen  = Specimen Holder

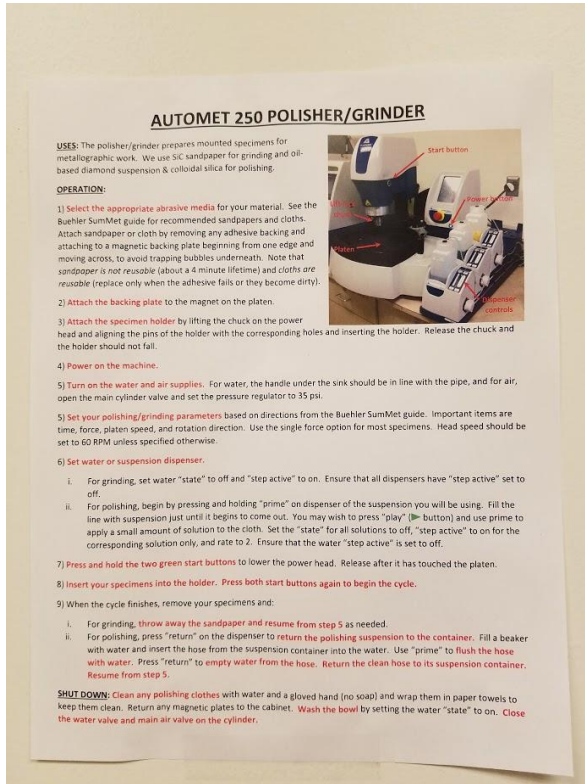


Figure 16: Instructions for AUTOMET 250 Polisher/Grinder.

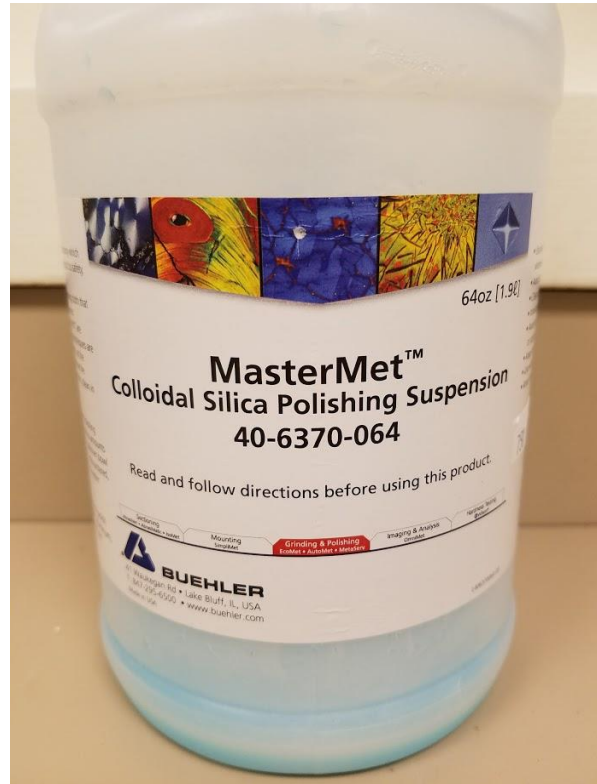


Figure 17: Colloidal silica solution.

Appendix B: Labeling System

This document contains the labeling system that the team used to label to test samples.

A - 6061 Perp.

B - 6061 Para.

C - 7075 Para.

D - 7075 Perp.

E - 2024 Para.

F - 2024 Perp.

G - A356-UM 500GS 60um

H - A356-UM 500GS 100um

I - A356+Sr 500GS 60um

J - A356+Sr 500GS 85um

K - A356-UM 1300GS 60um

L - A356-UM 1300GS 100um

M - A356+Sr 1300GS 60um

N - A356+Sr 1300GS 100um

O - 319-UM 1300GS 60um

P - 319-UM 1300GS 85um

Q - 319+Sr 1300GS 60um

R - 319+Sr 1300GS 85um

S - 390-UM 1300GS

T - 390+P 1300GS

Appendix C: Measurements of Microstructural Characteristics

A356 Microhardness

A356 Samples	Vicker Hardness (100 N)
A356-UM 500 GS 60um, AF	55.47
A356-UM 500 GS 60um, 0hr	80.47
A356-UM 500 GS 60um, 1.5hr	74
A356-UM 500 GS 60um, 4hr	80.65
A356-UM 500 GS 60um, 8hr	93.25
A356-UM 500 GS 60um, 16hr	92.31
A356-UM 500 GS 100um, AF	N/A
A356-UM 500 GS 100um, 0hr	68.24
A356-UM 500 GS 100um, 1.5hr	61.49
A356-UM 500 GS 100um, 4hr	61.98
A356-UM 500 GS 100um, 8hr	99.85
A356-UM 500 GS 100um, 16hr	85.68
A356+Sr 500 GS 60um, AF	61.44
A356+Sr 500 GS 60um, 0hr	74.14
A356+Sr 500 GS 60um, 1.5hr	75.73
A356+Sr 500 GS 60um, 4hr	76.6
A356+Sr 500 GS 60um, 8hr	87.87
A356+Sr 500 GS 60um, 16hr	111.8
A356+Sr 500 GS 85um, AF	58.19
A356+Sr 500 GS 85um, 0hr	64.15
A356+Sr 500 GS 85um, 1.5hr	79.01
A356+Sr 500 GS 85um, 4hr	89.52

A356+Sr 500 GS 85um, 8hr	88.85
A356+Sr 500 GS 85um, 16hr	91.23
A356-UM 1300 GS 60um, AF	59.74
A356-UM 1300 GS 100um, AF	54.68
A356+Sr 1300 GS 60um, AF	59.79

319 Microhardness

319 Samples	Vicker Hardness (100 N)
319+Sr 1300 GS 60um, AF	72.90
319+Sr 1300 GS 85um, AF	77.92

Wrought Alloys Microhardness

Wrought Alloy & Direction	Vicker Microhardness (100 N)
6061 YZ	146.1
6061 XY	160.8
6061 XZ	154.7
7075 YZ	165.5
7075 XY	167.1
7075 XZ	156.3

A356 SDAS & Eutectic Si Morphology

A356 Samples	SDAS (μm)	Equivalent Diameter (μm)	Aspect Ratio (W/L)	Shape Factor
A356-UM 500 GS 60um, AF	63.79	4.07	0.0927	0.791
A356-UM 500 GS 60um, 0hr		6.37	0.138	0.865
A356-UM 500 GS 60um, 1.5hr		7.13	0.1063	0.626
A356-UM 500 GS 60um, 4hr		7.47	0.1002	0.632
A356-UM 500 GS 60um, 8hr		7.28	0.907	0.627
A356-UM 500 GS 60um, 16hr		7.54	0.1092	0.728
A356-UM 500 GS 100um, AF		8.92	0.0316	0.596
A356-UM 500 GS 100um, 0hr		8.11	0.074	0.7
A356-UM 500 GS 100um, 1.5hr		7.84	0.0719	0.703
A356-UM 500 GS 100um, 4hr		7.43	0.0705	0.72
A356-UM 500 GS 100um, 8hr		9.12	0.0812	0.623
A356-UM 500 GS 100um, 16hr		2.22	0.1627	1.014
A356+Sr 500 GS 60um, AF		4.28	0.1245	0.837
A356+Sr 500 GS 60um, 0hr		2.51	0.1896	0.895
A356+Sr 500 GS 60um, 1.5hr		2.07	0.2111	0.856
A356+Sr 500 GS 60um, 4hr		2.59	0.0927	0.87
A356+Sr 500 GS 60um, 8hr		2.51	0.1927	0.919
A356+Sr 500 GS 60um, 16hr		2.72	0.108	0.858
A356+Sr 500 GS 85um, AF		3.191	0.0603	0.589
A356+Sr 500 GS 85um, 0hr		3.26	0.1725	0.827
A356+Sr 500 GS 85um, 1.5hr		3.48	0.1987	0.824

A356+Sr 500 GS 85um, 4hr		4.9	0.1635	0.859
A356+Sr 500 GS 85um, 8hr		4.7	0.1652	1.164
A356+Sr 500 GS 85um, 16hr		4.6	0.1652	0.835
A356-UM 1300 GS 60um, AF	61.39	4.22	0.087	0.751
A356-UM 1300 GS 100um, AF	98.28	4.54	0.0823	0.77
A356+Sr 1300 GS 60um, AF	60.82	1.83	0.2655	0.92

319 SDAS & Silicon Morphology

319 Samples	SDAS (μm)	Equivalent Diameter (μm)	Aspect Ratio (W/L)	Shape Factor
319-UM 1300 GS 85um, AF	N/A	10.94	0.0592	0.576
319+Sr 1300 GS 60um, AF	59.4	2.28	0.1593	0.697
319+Sr 1300 GS 85um, AF	86.87	4.13	0.1079	0.652

390 SDAS & Silicon Morphology

390 Samples	SDAS (μm)	Equivalent Diameter (μm)	Aspect Ratio (W/L)	Shape Factor
390 + P	N/A	5.00	0.0775	1.946
390 no P	N/A	13.21	0.0596	0.645

Appendix D: Thermal Conductivity Measurements

A356 Thermal Conductivities

A356 Samples	Thermal Conductivity (W/(m*K))
A356-UM 500 GS 60um, AF	153.20
A356-UM 500 GS 60um, 0hr	139.48
A356-UM 500 GS 60um, 1.5hr	154.58
A356-UM 500 GS 60um, 4hr	153.51
A356-UM 500 GS 60um, 8hr	150.69
A356-UM 500 GS 60um, 16hr	134.86
A356-UM 500 GS 100um, AF	79.97
A356-UM 500 GS 100um, 0hr	71.22
A356-UM 500 GS 100um, 1.5hr	150.31
A356-UM 500 GS 100um, 4hr	156.22
A356-UM 500 GS 100um, 8hr	152.70
A356-UM 500 GS 100um, 16hr	152.83
A356+Sr 500 GS 60um, AF	168.15
A356+Sr 500 GS 60um, 0hr	125.47
A356+Sr 500 GS 60um, 1.5hr	155.99
A356+Sr 500 GS 60um, 4hr	137.25
A356+Sr 500 GS 60um, 8hr	189.01
A356+Sr 500 GS 60um, 16hr	197.73
A356+Sr 500 GS 85um, AF	161.56
A356+Sr 500 GS 85um, 0hr	178.52
A356+Sr 500 GS 85um, 1.5hr	190.51
A356+Sr 500 GS 85um, 4hr	177.98

A356+Sr 500 GS 85um, 8hr	130.88
A356+Sr 500 GS 85um, 16hr	167.42
A356-UM 1300 GS 60um, AF	156.92
A356-UM 1300 GS 60um, 0hr	160.07
A356-UM 1300 GS 60um, 1.5hr	161.24
A356-UM 1300 GS 60um, 4hr	172.66
A356-UM 1300 GS 60um, 8hr	151.10
A356-UM 1300 GS 60um, 16hr	174.18
A356-UM 1300 GS 100um, AF	88.10
A356-UM 1300 GS 100um, 0hr	163.34
A356-UM 1300 GS 100um, 1.5hr	159.11
A356-UM 1300 GS 100um, 4hr	170.62
A356-UM 1300 GS 100um, 8hr	99.55
A356-UM 1300 GS 100um, 16hr	157.41
A356+Sr 1300 GS 60um, AF	196.56
A356-UM 1300 GS 100um, 0hr	179.66
A356-UM 1300 GS 100um, 1.5hr	159.36
A356-UM 1300 GS 100um, 4hr	150.91
A356-UM 1300 GS 100um, 8hr	115.96
A356-UM 1300 GS 100um, 16hr	120.38

319 Thermal Conductivities

319 Samples	Thermal Conductivity (W/(m*K))
319-UM 1300 GS 60um, AF	150.00
319+Sr 1300 GS 60um, AF	142.11
319+Sr 1300 GS 85um, AF	133.82

Wrought Alloy Thermal Conductivities

Wrought Samples	Thermal Conductivity (W/(m*K))
6061 Para.	90.60
6061 Perp.	67.20
7075 Para.	93.26
7075 Perp.	58.27

Appendix E: Electrical Conductivity Measurements

A356 Electrical Conductivities

A356 Samples	Electrical Conductivity (S/m)	Electrical Conductivity (%IACS)
A356-UM 500 GS 60um, AF	3.61×10^6	6.22
A356-UM 500 GS 100um, AF	8.31×10^6	14.33
A356+Sr 500 GS 60um, AF	4.46×10^6	7.69
A356+Sr 500 GS 85um, AF	8.07×10^6	13.91
A356-UM 1300 GS 60um, AF	8.98×10^6	15.49
A356-UM 1300 GS 100um, AF	1.10×10^7	18.94
A356+Sr 1300 GS 60um, AF	1.78×10^7	30.69

319 Electrical Conductivities

319 Samples	Electrical Conductivity (S/m)	Electrical Conductivity (%IACS)
319-UM 1300 GS 60um, AF	1.42×10^7	24.53
319+Sr 1300 GS 60um, AF	1.19×10^7	20.58
319+Sr 1300 GS 85um, AF	6.68×10^6	11.52

Wrought Alloy Electrical Conductivities

Wrought Samples	Electrical Conductivity (S/m)	Electrical Conductivity (%IACS)
6061 Para.	7.18×10^6	12.37
6061 Perp.	5.11×10^6	8.81
7075 Para.	2.44×10^6	4.21
7075 Perp.	2.33×10^6	4.02